RESEARCH ARTICLE
PLANETARY SCIENCES

Earth and Planetary Physics
7: 311–330, 2023
doi: 10.26464/epp2023044

Phenomenology of plume–surface interactions and preliminary results from the Tianwen-1 landing crater on Mars

Tao Xu[1,3,4], Bo Zheng[1,3,4], ZhaoBin Zhang[1,3,4], Juan Li[2,3,4*], ShouDing Li[1,3,4*], XinShuo Chen[1,3,4], XiuKuo Sun[1,3,4], YanFang Wu[1,3,4], and YiMing Diao[1,3,4]

[1]Key Laboratory of Shale Gas and Geoengineering, Institute of Geology and Geophysics, Chinese Academy of Sciences, Beijing 100029, China;

[2]Key Laboratory of Earth and Planetary Physics, Institute of Geology and Geophysics, Chinese Academy of Sciences, Beijing 100029, China;

[3]College of Earth and Planetary Sciences, University of Chinese Academy of Sciences, Beijing 100049, China;

[4]Innovation Academy for Earth Sciences, Chinese Academy of Sciences, Beijing 100029, China

Key Points:

- The phenomenology and erosion mechanisms of plume–surface interactions (PSI) were analyzed, and the evolution of PSI terrestrial tests was reviewed.
- The deepest landing crater (depth > 40 cm) was caused by the PSI of Tianwen-1 and exposed stratigraphic layering in the subsurface.
- Martian soil mechanical properties were weakly constrained by the slope stability analysis of the Tianwen-1 landing crater.

Citation: Xu, T., Zheng, B., Zhang, Z. B., Li, J., Li, S. D., Chen, X. S., Sun, X. K., Wu, Y. F., and Diao, Y. M. (2023). Phenomenology of plume–surface interactions and preliminary results from the Tianwen-1 landing crater on Mars. *Earth Planet. Phys.*, *7*(3), 311–330. http://doi.org/10.26464/epp2023044

Abstract: The plume–surface interaction (PSI) is a common phenomenon that describes the environment surrounding the landers resulting from the impingement of hot rocket exhaust on the regolith of planetary bodies. The PSI will cause obscuration, erosion of the planetary surface, and high-speed spreading of dust or high-energy ejecta streams, which will induce risks to a safe landing and cause damage to payloads on the landers or to nearby assets. Safe landings and the subsequent scientific goals of deep-space exploration in China call for a comprehensive understanding of the PSI process, including the plume flow mechanics, erosion mechanism, and ejecta dynamics. In addition, the landing crater caused by the plume provides a unique and insightful perspective on the understanding of PSI. In particular, the PSI can be used directly to constrain the composition, structure, and mechanical properties of the surface and subsurface soil. In this study, we conducted a systematic review of the phenomenology and terrestrial tests of PSI: we analyzed the critical factors in the PSI process and compared the differences in PSI phenomena between lunar and Martian conditions; we also reviewed the main erosion mechanisms and the evolution and development of terrestrial tests on PSI. We discuss the problems with PSI, challenges of terrestrial tests, and prospects of PSI, and we show the preliminary results obtained from the landing crater caused by the PSI of Tianwen-1. From analysis of the camera images and digital elevation model reconstructions, we concluded that the landing of Tianwen-1 caused the deepest crater (depth > 40 cm) on a planetary surface reported to date and revealed stratigraphic layers in the subsurface of Martian soil. We further constrained the lower bounds of the mechanical properties of Martian soil by a slope stability analysis of the Tianwen-1 landing crater. The PSI may offer promising opportunities to obtain greater insights into planetary science, including the subsurface structure, mineral composition, and properties of soil.

Keywords: plume–surface interaction; phenomenology analysis; terrestrial test; Tianwen-1; landing crater

1. Introduction

The plume–surface interaction (PSI) is a complex multiphase and multisystem discipline that describes the environment surrounding the landers resulting from the impingement of hot rocket exhaust on the regolith of planetary bodies (Figure 1). This environment is characterized by plume flow physics, cratering physics, and ejecta dynamics (Mehta, 2019). The impinging exhaust gas generates a strong recirculation region that fluidizes the surface and ejects loose granular matter. Plume–surface interactions cause risks, including destabilizing the lander module and dislodging dust and debris at high speeds that can damage exposed hardware, reduce visibility, and spoof landing sensors. The China National Space Administration (CSNA), the National Aeronautics and Space Administration (NASA), and the European Space Agency (ESA) are actively implementing a series of planetary exploration missions (Table 1). Their exploration targets mainly include the Moon, Mars, and other extraterrestrial objects.

First author: T. Xu, xutao19@mails.ucas.ac.cn
Correspondence to: J. Li, juanli@mail.iggcas.ac.cn
S. D. Li, lsdlyh@mail.iggcas.ac.cn
Received 20 JAN 2023; Accepted 27 APR 2023.
Accepted article online 06 MAY 2023.

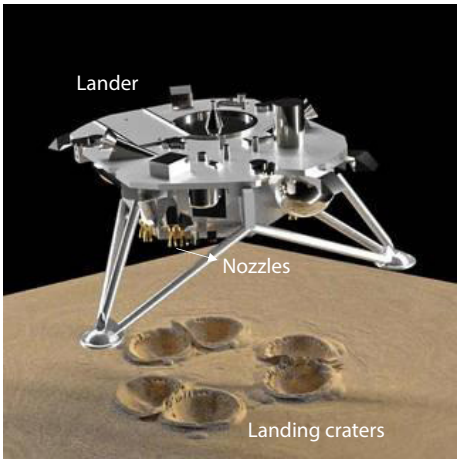

Figure 1. The typical phenomenon of the plume–surface interaction (PSI) during the landing process. Base map from the NASA PSI project.

The landing process is one of the most critical stages during the atmospheric entry, descent, and final landing process (known as EDL), as it affects the exploration mission (Yu ZS et al., 2017). Because of the communication delay, the landing platforms must navigate automatically during the landing process. Regular landing modes operate in three typical ways: airbags, retro-rockets, or sky cranes (Figure 2). The first landing mode is the airbags, which are adopted when the landers are relatively light, such as those used by the Pathfinder (Golombek, 1997) and the Spirit and Opportunity rovers (Arvidson,et al., 2004a; Arvidson et al., 2006). The airbag inflates the lander, lands, and rolls on the extraterrestrial surface. Because of the uncertainty of rolling, however, the landing accuracy is inadequate (Figure 2a). The second landing mode depends on the retro-rocket engines and the lander legs when the mass is less than 0.6 tons. In this case, the ballistic coefficient should be less than 35 kg/m^2, the diameter of the aeroshell less than 4.6 m, the geometry of the aeroshell a 70° spherical cone shell, and the diameter of the parachute less than 30 m (Braun and Manning, 2007). The retro-rocket engines are below the lander module, and the engines are ignited when the lander is close to the surface. The landing then continues in a power deceleration phase until the lander modules touch the surface (Figure 2b). The retro-rocket was adopted by the Apollo missions (Hinners and El-Baz, 1972; Immer et al., 2011a; Clegg et al., 2012), the Surveyor missions (Chen JL, 2014), Viking-1, Viking-2 (Clark, 1970a; Romine et al., 1973; Hutton et al., 1980), InSight (Banerdt et al., 2020), Chang'e-3/4/5 (Li CL et al., 2015; Liu ZQ et al., 2020; Wang J et al., 2021), and Tianwen-1 (Zou YL et al., 2021; Xu C et al., 2022; Huang H et al.,

Table 1. Typical planetary exploration mission information.

	Mission[a]	Country	Year	Landing mode	Landing mass (kg)	Landing site	
Mars	Mars 3	Soviet	1971	Retro-rockets	1,210	Sirenum Terra	45°S 158°W
	Mars 6	Soviet	1973	Retro-rockets	635	Margaritifer Terra	23.90°S 19.42°W
	Viking 1	USA	1976	Retro-rockets	657	Chryse Planitia	22.697°N 48.222°W
	Viking 2	USA	1976	Retro-rockets	657	Utopia Planitia	48.269°N 225.990°W
	Pathfinder	USA	1996	Airbags	Rover: 11.5 Lander: 360	Ares Vallis	19.3300°N 33.5500°W
	Beagle 2	UK	2003	Failed	33.2	Isidis Planitia	11.5265°N 90.4295°E
	Spirit	USA	2004	Airbags	185	Gusev Crater	14.5718°S 175.4785°E
	Opportunity	USA	2004	Airbags	185	Meridiani Planum	1.9462°S 354.4734°E
	Phoenix	USA	2007	Retro-rockets	350	Green Valley	68.2188°N 125.7492°W
	Curiosity	USA	2011	Sky crane	900	Gale Crater	4.5895°S 137.4417°E
	InSight	USA	2018	Retro-rockets	358	Elysium Planitia	4.5024°N 135.6234°E
	Perseverance	USA	2020	Sky crane	1,025	Jezero Crater	18.4457°N 77.4508°E
	Tianwen-1	China	2021	Retro-rockets	Zhurong: 240 Lander: 1,285	Utopia Planitia	25.066°N 109.925°E
The Moon	Chang'e 3	China	2013	Retro-rockets	Yutu: 140	Mare Imbrium	44.1214°N 19.5116°W
	Chang'e 4	China	2018	Retro-rockets	Yutu-2: 140	Von Kármán crater	45.4561°S 177.5885°E
	Chang'e 5	China	2020	Retro-rockets	>882	Mons Rümker	43.0576°N 51.9161°W

[a]Mars 3: https://nssdc.gsfc.nasa.gov/nmc/spacecraft/display.action?id=1971-049A; Mars 6: https://nssdc.gsfc.nasa.gov/nmc/spacecraft/display.action?id=1973-052A; Viking 1: https://nssdc.gsfc.nasa.gov/nmc/spacecraft/display.action?id=1975-075C; Viking 2: https://nssdc.gsfc.nasa.gov/nmc/spacecraft/display.action?id=1975-083C; Pathfinder: https://nssdc.gsfc.nasa.gov/nmc/spacecraft/display.action?id=1996-068A; Spirit and Opportunity: http://www.esri.com/news/arcuser/0404/mapmars3of3.html; Phoenix: https://www.jpl.nasa.gov/news/press_kits/phoenix-launch-presskit.pdf; Curiosity: http://solarsystem.nasa.gov/docs/MSL_Landing_20120724.pdf; InSight: https://www.jpl.nasa.gov/news/press_kits/insight/launch/download/mars_insight_launch_presskit.pdf; Perseverance: https://www.jpl.nasa.gov/news/press_kits/mars_2020/download/mars_2020_landing_press_kit.pdf; Beagle-2: Bridges et al. (2017); Chang'e 3: Liu ZQ et al. (2015); Chang'e 4: Liu ZQ et al. (2020); Chang'e 5: Wang J et al. (2021); Tianwen-1: Liu JJ et al. (2022).

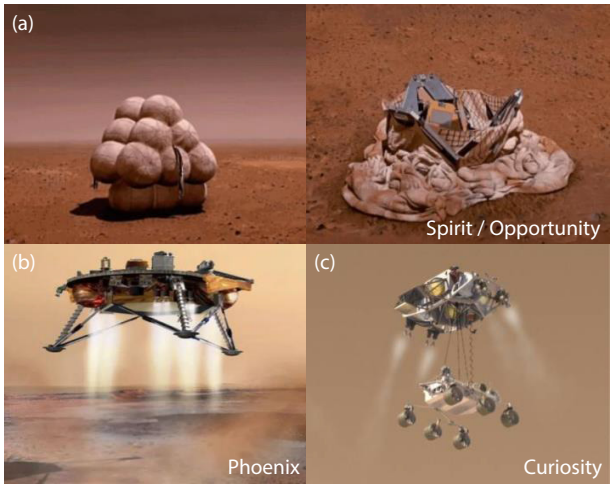

Figure 2. Typical landing modes of the probe lander. (a) Airbags; (b) retro-rockets; (c) sky crane. Photo credit: NASA.

2023). The third landing mode is the sky crane. The retro-rocket engines of the sky crane are ignited to achieve hovering. The sky crane and lander will separate when the lander rover is sent to the ground by ropes. The sky crane is the most complicated mode because of its high landing accuracy and carrying capacity (Figure 2c). This mode was adopted by the Curiosity (Arvidson et al., 2014) and Perseverance rovers (Pla-García et al., 2020).

The retro-engines of the retro-rocket and the sky crane landing modes will cause severe risks of PSI during the missions (Figures 2b, c), and a safe landing is intensively influenced by the PSI (Hutton et al., 1980). Mitigating the danger of the PSI requires a comprehensive understanding of multiphase dynamics under supersonic and extra-high-temperature conditions (Watkins et al., 2021).

In addition, landing craters possibly form below or near the lander modules during the landing process (Metzger and Mantovani, 2021). Key information can be obtained directly from images of the landing craters, which may include information on shallow geological structures or the components and mechanical properties of the soil (Mehta et al., 2019). The dynamics of the cratering process involve high-speed, compressible gas–particle two-phase flows. The coupling interaction of the engine plume and the planetary surface involves fluid mechanics, solid mechanics, and geomechanics. The PSI also involves continuum flow and rarefied gas flow, soil failure, and particle transport or ejection (Figure 3).

To gain a better understanding of the entire PSI process, a series of research projects were carried out, aimed at relevant issues of PSI under planetary conditions (Kuhns et al., 2021; Fontes and Metzger, 2022). In this work, the phenomenology of PSI during the landing process on the Moon and Mars is systematically reviewed. Differences in PSI phenomena between lunar and Martian conditions are then compared, and the critical factors causing the differences are analyzed. On the basis of this analysis of PSI phenomena, five typical erosion mechanisms that describe the different reasons for erosion of the regolith are discussed further. In addition, the evolution and development of terrestrial test experiments on PSI are introduced, and the current challenges and prospects of terrestrial tests are analyzed. In addition, a preliminary study of the landing crater below the Zhurong rover was conducted, including its geometry and the mechanical properties of Martian soil. Plume–surface interaction phenomena may offer a promising opportunity to obtain new insights into planetary science, including the geological profile and properties of the soil.

2. Phenomenology of Planetary PSI

At present, the motivations for planetary missions are mainly to explore the Moon and Mars. Because of the differences between the Moon and Mars, including the atmospheric conditions (Table 2), surface physical properties (i.e., bulk density), mechanical properties of the regolith (i.e., internal friction angle and cohesion;

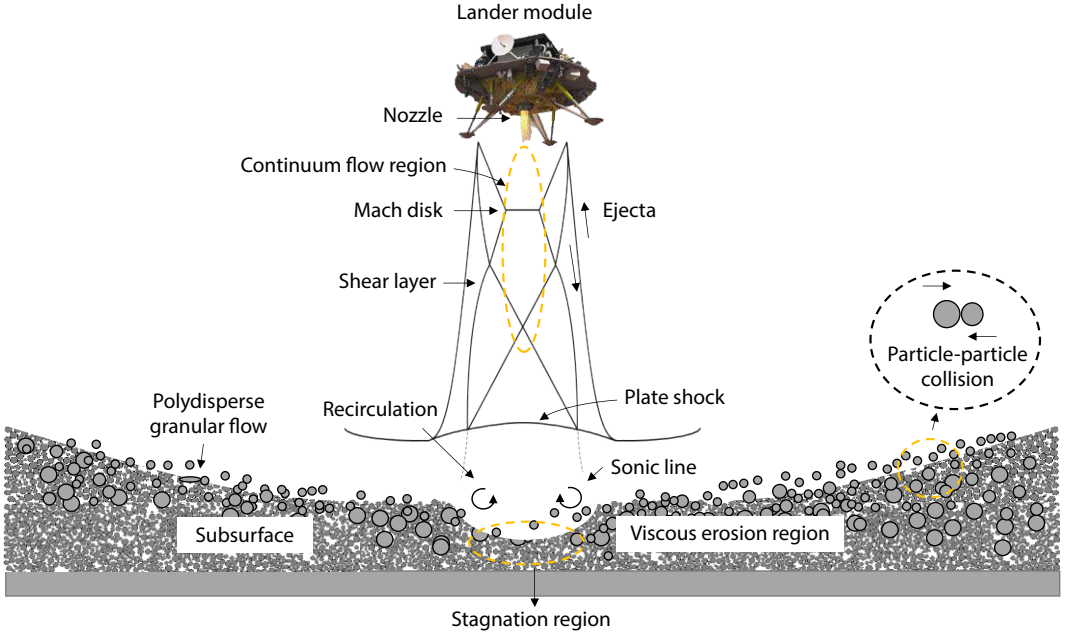

Figure 3. Schematic of plume–surface interactions. Modified from Rahimi et al. (2020) and Capecelatro (2022).

Table 2. Typical atmospheric conditions at the surface of the Earth, Moon, and Mars.

Parameter	Earth	Moon	Mars
Gravitational acceleration (m/s^2)	9.81	1.62	3.72
Surface pressure (Pa)	1.01×10^5	3×10^{-10}	500–700
Density (kg/m^3)	1.2	≈0	1.66×10^{-2}
Dynamic viscosity (N·s/m^2)	1.8×10^{-5}	—	1.5×10^{-5}
Speed of sound (m/s)	343	—	264

Figure 4), and the thrust engines, the phenomenology of PSI is different under the conditions of the Moon and Mars (Christensen et al., 1968; Metzger et al., 2009a; Shaw et al., 2009). Compared with landings on the Moon, where the vacuum permits the plume to spread over a wide area, the Martian landing process involves the possibility of severe soil disturbances within the finite Martian atmosphere. The specific phenomena of Martian and lunar PSI are introduced in the next two sections (Figure 5).

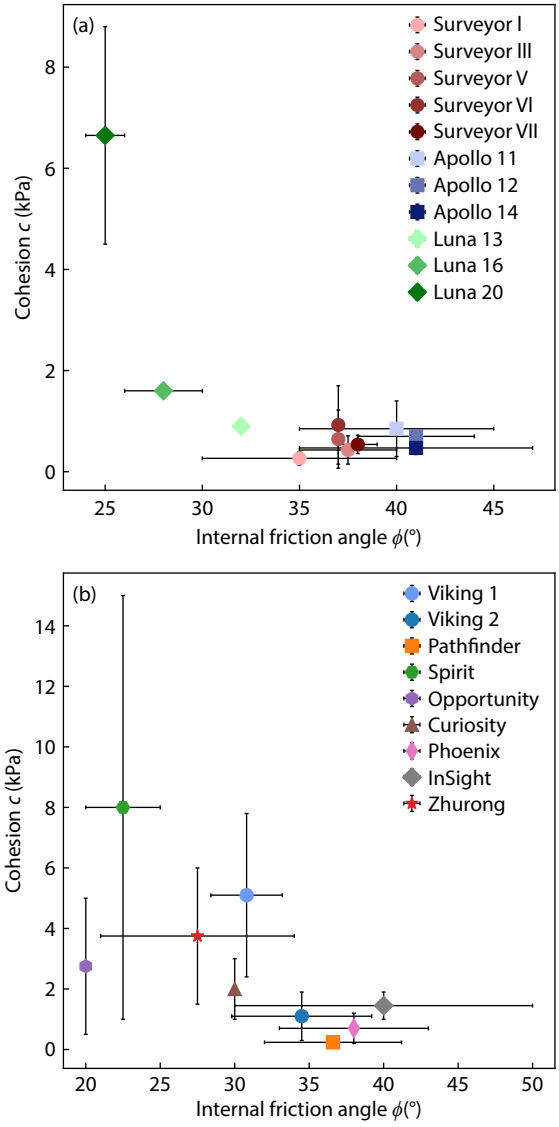

Figure 4. Typical planetary soil mechanical properties. Internal friction angle and cohesion on the Moon (a) and Mars (b). Data sources are shown in Table 3.

2.1 PSI on the Moon

According to data collected during the Luna, Surveyor, Apollo, and Chang'e exploration missions, the PSI phenomenon could be observed beginning at an altitude of 30–40 m above the surface of the Moon. It is noteworthy that PSI can cause crucial risks to missions, including damage to the lunar exploration modules and landing failures (Katzan and Edwards, 1991; Clegg et al., 2011, 2012; You JL et al., 2021; Zhang HY et al., 2022). The phenomenon of visibility being hampered by particles ejected from the PSI was observed in four of the six Apollo landings (Figures 6a–d).

Mason (1970) conducted a comparison of actual lunar surface erosion caused by Apollo 11 descent engines (Figure 6a) with results predicted by the erosion law and described the experiential relationships between the erosion volume of the regolith and the parameters of the engines. Photographic evidence and astronauts' descriptions suggested that only a small fraction of the regolith was eroded by the plume, which is consistent with the computed results from the empirically derived erosion law showing a maximum eroded depth of 1.27 cm. Immer et al. (2011a) analyzed the plume impingement by retro-rockets during the Apollo 12 landing process (Figure 6b). Visual inspection, scanning electron microscopy, and surface scanned topology have been utilized to study the damage to Surveyor III spacecraft components caused by PSI during the Apollo 12 landing process. From an analysis of two parts of Surveyor III returned by the crew on Apollo 12, the results of the impact on Coupons (components on Surveyor III) showed that the impact of soil particles caused an average pitted density of 103 pits/cm^2, that the average entry size of the pits was 83.7 μm (major diameter) × 74.5 μm (minor diameter), and that the average penetration depth was 88.4 μm. These data suggest that Surveyor III was exposed to the affected range of the landing of Apollo 12 on the Moon.

Suspended particles were detected in the modules about 11 m away from Apollo 11 and about 160 m away from Apollo 12. During the landing process of Apollo 12, a recessed location on the Surveyor's camera was contaminated with lunar fines (up to ~150-micron particles) where they had been blown through an inspection hole (Immer et al., 2011b). According to the statistical data, the velocity of particles exceeded 100 m/s, and the velocity of particles striking the Surveyor was between 300 and 2,000 m/s. In addition, the crew of Apollo 14 observed a crater along the landing trajectory (Figure 6c) just behind the final resting position of the nozzle (Katzan and Edwards, 1991). During the final seconds of the Apollo 15 landing process (Figure 6d), a dense blast of soil

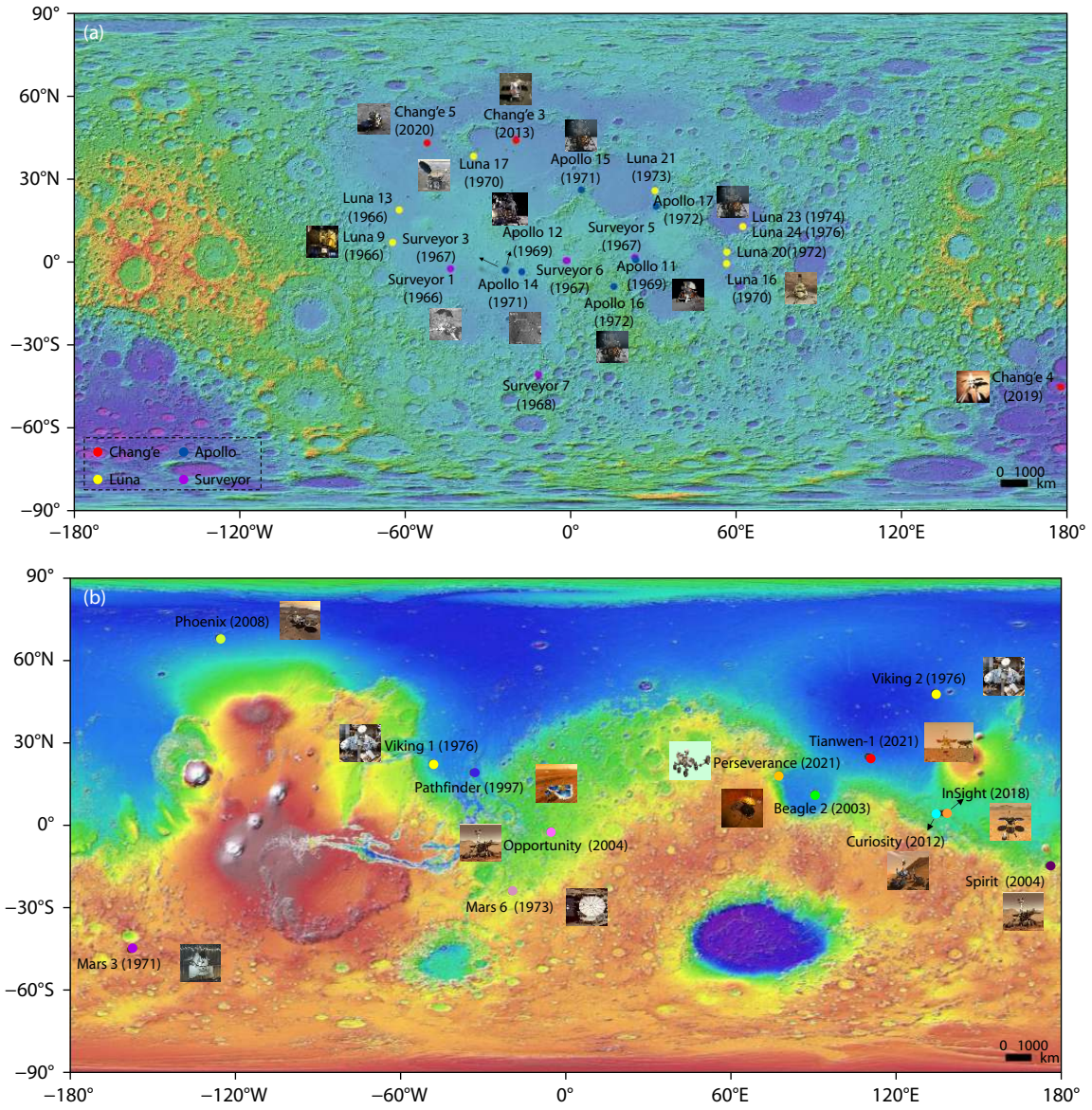

Figure 5. Distribution of typical landing sites. (a) The Moon; (b) Mars. Base map from the U.S. Geological Survey (https://planetarymaps.usgs.gov/mosaic/Lunar_LRO_LOLA_ClrShade_Global_128ppd_v04.tif and https://planetarymaps.usgs.gov/mosaic/Mars_MGS_MOLA_ClrShade_merge_global_463m.tif).

sent ejecta to approximately 22°. The landing module experienced a sharp incline close to 12°, which almost aborted the mission (McDivitt, 1971). Because of the vacuum condition of the Moon, the smaller particles suspended during the Apollo landing were estimated to have reached escape velocity, posing a hazard to orbital hardware (Lane et al., 2008). According to the Apollo lunar descent images (Figure 6e), the lunar dust stirred up by the plume contained 10^8–10^{13} particles/m^3, and the ejection angle of the blown particles was 1°–3°. The visibility was intensely affected by the brown dust, and rocks exceeding 10 cm in size were possibly moved by the engine plume near the Apollo landing area (Metzger et al., 2011). Because of the physical and mechanical properties of the lunar regolith, the surficial cratering process was inconspicuous, according to the images from the Chang'e 4 (Figure 6f), and some small pits around 0.7 cm in size were observed (You JL et al., 2021). The Chang'e 5 recorded information during the landing process as well. The variation in landing images with landing time is illustrated in Figure 6g. During the landing period, the nozzle altitude changed from approximately 94 m to 0.48 m. The corresponding landing photos show the brightest region below the nozzle outlet in the center of the photo, which indicates that a thick layer of lunar regolith was blown away by the plume (Zhang HY et al., 2022).

In addition, rocket exhaust from the descent engines disturbs the regolith at landing sites, causing the soil to become more reflective, which then causes surface alterations known as blast zones. Clegg et al. (2016) analyzed the spacecraft dry mass (spacecraft mass without fuel), thrust, and blast zone area of global lunar missions. The relationship between dry mass and blast zone area was then analyzed, and a quadratic fitting curve with 95% confidence was obtained (Figure 7a). Although the number of engines and the design of the thrust engines were different in these

Table 3. Typical properties of the soil on the Moon and Mars.

Mission	Cohesion c (kPa)	Internal friction angle φ (°)	Bulk density ρ (g/cm^3)	Test method
Surveyor I	0.13–0.40	30–40	1.50	Footpad penetration (Christensen et al., 1967a)
Surveyor III	0.15–0.71	35–40	1.50	Scoop test (Scott and Roberson, 1968)
Surveyor V	0.07–1.22	37	—	Footpad penetration (Christensen et al., 1967b)
Surveyor VI	0.15–1.70	37	—	Footpad penetration (Christensen, 1970)
Surveyor VII	0.36–0.72	37–39	1.50	Scoop test (Roberson and Scott, 1968)
Apollo 11	0.30–1.40	35–45	0.74–2.00	Footprints/crater slope stability/penetration/ landing data (Costes et al., 1970)
Apollo 12	0.60–0.80	38–44	1.55–1.90	Footprints/crater slope stability/penetration/ landing data (Scott et al., 1971)
Apollo 14	0.34–0.60	35–47	1.45–1.60	Penetrometer/wheel (Mitchell et al., 1972)
Luna 13	0.90	32	0.80	Penetrometer (Cherkasov et al., 1969)
Luna 16	1.60	26–30	1.20	Sample testing (Surkov et al., 1975)
Luna 17	4.00–5.00	—	—	Cone penetration (Leonovich et al., 1971)
Luna 20	4.50–8.80	24–26	—	Sample testing (Leonovich et al., 1976)
Luna 21	—	20–24	—	Cone penetration (Johnson and Chua, 1993)
Viking 1	5.10 ± 2.70	30.8 ± 2.4	1.15 ± 0.15	Footpad penetration (Moore and Jakosky, 1989)
Viking 2	1.10 ± 0.80	34.5 ± 4.7	1.40 ± 0.20	Footpad penetration (Moore and Jakosky, 1989)
Pathfinder	0.12–0.36	32–41	1.29–1.64	Rover wheel (Team, 1997)
Spirit	~1.00–15.00	~20–25	1.20–1.5	Rover wheel (Arvidson et al., 2004a)
Opportunity	~0.50–5.00	~20	~1.3	Rover wheel (Arvidson et al., 2004b)
Curiosity	1.00–3.00	~30	—	Rover wheel (Arvidson et al., 2014)
Phoenix	0.20–1.20	38 ± 5	1.24	Scoop test (Shaw et al., 2009)
InSight	>1.00–1.90	30–50	1.10–1.36	Landing crater (Golombek et al., 2020)
Zhurong	1.50–6.00	~21–34	—	Rover wheel (Ding L et al., 2022)

missions (single engine or multiple engines and engine configurations), the relationship between the maximum thrust of a single engine and the blast zone area was also consistent with a quadratic curve to some extent. The authors concluded that a larger maximum thrust resulted in a larger blast zone area. The same maximum thrust could result in different blast zone areas because of the different surficial regolith on the lunar landing sites (Figure 7b).

In general, the engine plume conditions of Apollo and Chang'e seemed to cause only small- to medium-sized craters or scour holes. According to the images above, which were transferred by the cameras on the landing platforms or rovers, the PSI on the Moon would not cause a deep and wide landing crater (approximately tens of centimeters), but the loose and uncompacted lunar regolith would be blown away and ejected.

2.2 PSI on Mars

When we compared the PSI phenomenon of Mars with that on the Moon, the PSI of Mars was distinct, and the dominant erosion mechanisms were possibly different (Hutton et al., 1980; Mehta et al., 2013). The PSI phenomena could differ for several possible reasons. The first and most crucial reason is that the soil properties on Mars and the Moon, such as the mechanical strength and porosity, are distinct. Second, the thin (but finite) Martian atmosphere inhibits the spread of exhaust gas, resulting in collimated rocket plumes that generate highly localized impingement pressures and deep craters (Mehta et al., 2013). Third, the thrust engines of the Martian modules differ from those of the lunar modules, which caused the plume modes and erosion mechanisms to differ. Fourth, the temperature fluctuations between day and night are different on Mars and the Moon. The temperature difference on Mars is in the range of −143°C to 35°C (Leovy, 2001), whereas that on the Moon is −183°C to 127°C (Williams et al., 2017).

To date, several Martian missions have been completed successfully. Before the Viking mission was implemented, an unacceptably violent bearing capacity failure was found, which was caused by the previous engine design in the soil sampling area. Therefore, the spacecraft engine was redesigned, and the single nozzle was replaced by a "showerhead" design with 18 tiny nozzles. The occurrence of a cluster of shallow craters corresponding to each of the individual nozzles was later confirmed, based on the images transferred by the Viking rovers (Figures 8a, b). In the Phoenix mission (Figure 8c), surficial patches of soil were cleared

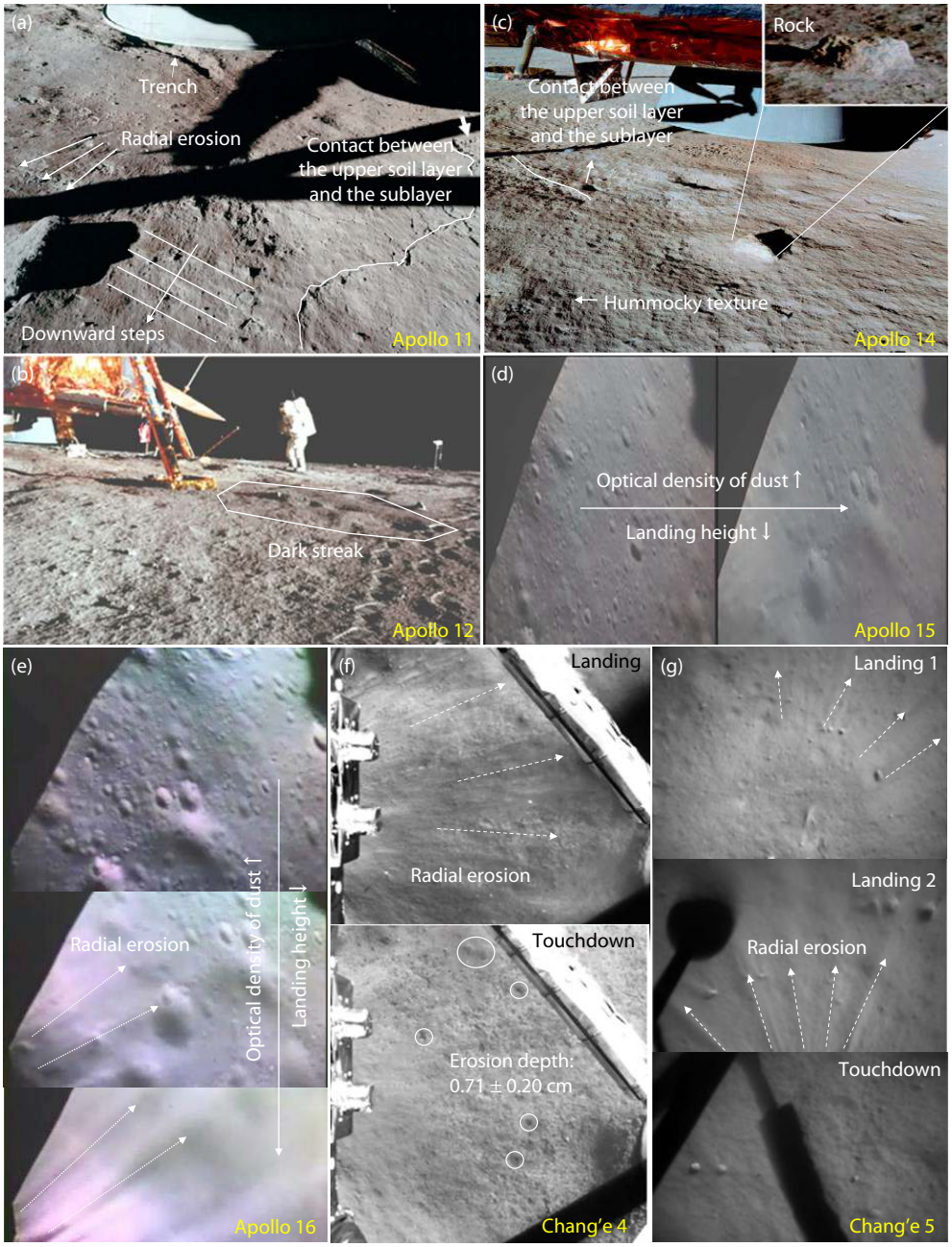

Figure 6. Phenomenology of plume–surface interactions on the Moon. (a) Apollo 11: The curve shows the contact between the upper soil layer and the sublayer. The figure also shows the radial erosion, downward steps, and trench caused by the plume (Metzger et al., 2011). (b) Apollo 12: The figure shows a dark streak (polygon) oriented radially away from Apollo 12 (Metzger et al., 2011). (c) Apollo 14: The curve shows the contact between the upper soil layer and the sublayer. The hummocky texture was caused by the plume in the figure. The inset shows a rock embedded in the ground (Metzger et al., 2011). (d) Apollo 15: Two frames of the landing video show an increase in the optical density of dust during the landing. (e) Apollo 16: Three frames of the landing video show an increase in the optical density of dust during the landing (Metzger et al., 2010). (f) Chang'e 4: The landing frame shows radial erosion. The erosion depth was 0.71 ± 0.20 cm after touchdown of the lander (You JL et al., 2021). (g) Chang'e 5: Three landing frames show radial erosion caused by the plume (Zhang HY et al., 2022). Base images from the China National Space Administration (Chang'e 4: F3362, F3377, and F3400; Chang'e 5: Nos. 417, 418, and 419) and the National Aeronautics and Space Administration (AS11-40-5921HR, AS12-46-6779HR, AS14-66-9266HR, and AS12-48-7034HR); contrast enhanced.

away by the Phoenix's 12 engines (with 30% less total thrust) pulsating at 10 Hz with an average impingement pressure of only 1/10 of the Earth's sea level pressure (Rennó et al., 2009). It is noteworthy that the subsurface ice under the lander platform was exposed several centimeters below the surface over a radius of 75 to 85 cm (Smith et al., 2009), which suggests the possibility that the engine plume may have induced deep cratering in the Martian regolith (Mehta et al., 2011).

After the Phoenix mission, a novel landing mode for mitigating the risks of PSI, namely, the sky crane, was adopted by the Mars

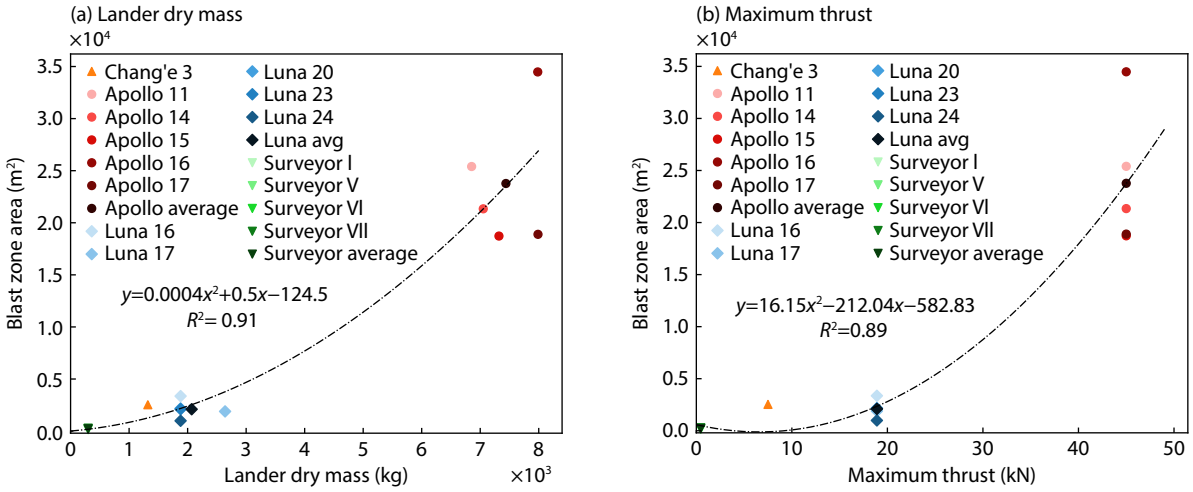

Figure 7. Relationship between the landers and the blast zone area. (a) Lander dry mass; (b) maximum thrust of a single engine. Note: The data from the Surveyor missions coincide. Data cited from Clegg et al. (2016).

Science Laboratory (MSL; Figure 8d). When the lander platform touches the ground, the thrusters of the sky crane remain high above the ground. According to data collected by the MSL, four typical craters were observed. The maximum crater depth, average diameter, eroded volume, and average erosion rate were 10.67 cm, 224.03 cm, 84,671.96 cm^3, and 4.27 kg/s, respectively (Arvidson et al., 2014). The next NASA Martian mission was InSight in 2018 (Figure 8e). The plume of the landing thrusters formed three craters below the lander platform. The average diameter of the three craters was 53.34 cm, and the average depth was 17.78 cm. Compared with the erosion rate of the MSL mission, the erosion rate of InSight (22.8 kg/s) was five times greater for two critical reasons: the pulse-modulated engines and the landing site, with its loose and deep regolith (Mehta, 2019). The sky crane landing mode was also adopted by Perseverance (Figure 8f), the same as for Curiosity. Cameras logged the violent erosion of Martian soil, and even the ejection of large rocks, during the landing of the Perseverance rover (Capecelatro, 2022). In the same period as the

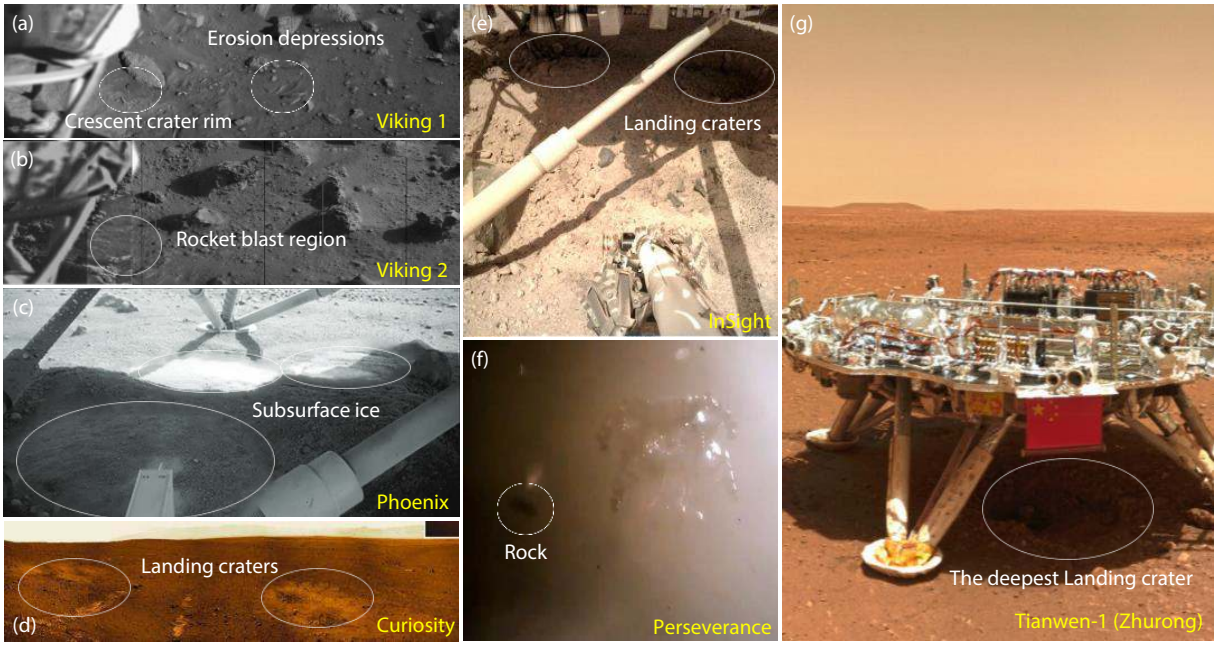

Figure 8. The phenomenology of plume–surface interactions (PSI) on Mars. (a) Viking-1: The figure shows some crescent crater rim and erosion depressions caused by the plume. (b) Viking-2: The figure shows a rocket blast region. (c) Phoenix: PSI revealed the subsurface ice below the Martian regolith (RS005EFF896663219_11730MDM1). (d) Curiosity: The engines of the sky crane caused landing craters (NLA_398919509EDR_F0030078NCAM00300M1). (e) InSight: The engine of the retro-rocket caused landing craters (https://photojournal.jpl.nasa.gov/catalog/PIA23301). (f) Perseverance: The engines of the sky crane caused the ejection of rocks. (g) Tianwen-1 (Zhurong): The deepest landing crater (> 40 cm) was caused by the retro-rocket of Tianwen-1 and a columnar-like rock block (height: ~15 cm) at the bottom of the landing crater. Based on images from the China National Space Administration and the National Aeronautics and Space Administration/Jet Propulsion Laboratory-Caltech; contrast enhanced.

Perseverance, Tianwen-1 carrying the Zhurong rover landed on Mars (Figure 8g). A retro-rocket engine was used to achieve a safe landing, which caused severe erosion of the Martian soil below the lander platform. A single deep crater (> 24 cm) was observed according to an image captured by the Zhurong rover (Ding L et al., 2022; Wu B et al., 2022). Conspicuous gas–particle interactions occurred during the descent of the lander platform.

3. Terrestrial Tests of PSI

3.1 PSI Erosion Mechanism

The typical PSI phenomena on Mars and the Moon described above are complicated. The PSI consists of approximately two stages: the failure of soil and the transport of soil particles. The first stage is the failure mechanism of planetary soil under the impingements of the engine plume. When the plume of the engines impinges on the surface soil, the original soil structures are destroyed by the extraneous forces in excess of the bulk strength of the soil. The current rationale utilizes the Mohr–Coulomb criterion (Equation (1)) to evaluate the failure of the soil. When the shear stress provided by the plume is in excess of the bulk shear strength of the soil, destruction of the soil occurs:

$$\tau_n = \sigma_n \tan\varphi + c, \tag{1}$$

where τ_n is the shear stress on the slip surface (Pa), σ_n is the normal stress on the slip surface (Pa), φ is the internal friction angle of the soil (°), and c is cohesion of the soil (Pa).

After the destruction of the soil structure, the soil particles are separated from the parent body of origin and are removed from their initial positions. The soil particles are raised aloft by the plume and then dispersed in the atmosphere. Notably, partial particles or rock blocks obtain a high speed that is sufficient to damage the surrounding equipment. The second stage is the transport of soil particles described by the Navier–Stokes equation (Equation (2)):

$$\frac{\partial \boldsymbol{V}}{\partial t} + (\boldsymbol{V}\cdot\nabla)\boldsymbol{V} = f - \frac{1}{\rho}\nabla p + \frac{\mu}{\rho}\nabla^2\boldsymbol{V}, \tag{2}$$

where $\boldsymbol{V}$ is the vector of velocity (m/s), t is time (s), f is the extraneous force per unit volume of fluid (N), ρ is density of fluid (kg/m^3), p is pressure (Pa), and μ is the dynamic viscosity (Pa·s).

According to the two stages above, some strategic knowledge gaps regarding the PSI mechanisms still exist. First, the size distributions, volumes, and velocities of particles ejected by the exhaust plumes need to be clarified. The transport distance of soil particles is also a critical indicator in evaluating the range of the PSI. Second, the distribution and altitude of the dust lifted after the engines are shut down are noteworthy; these include the duration of dust suspension, ejection mass, and particle size. A third crucial question is predicting the dynamic physical change of the landing site surface. Fourth, the physical models and quantitative relationships describing the effects on PSI of the lander size, engine configuration, and landing terrains are unclear (Watkins et al., 2021). In addition, other questions related to a safe landing should be addressed further, based on the answers to the previous questions.

According to fluid mechanics, the physical and chemical processes of the engine plume during landings could be precisely described by the Navier–Stokes equation. Because of the lack of reliable theoretical models that describe the failure and transport of soil ejected by the plume on the Moon or Mars, a precise prediction of cratering and particle transport is an enormous challenge in PSI research. The difficulties arise mainly for two reasons (Figure 9). The quantitative relationship between the engineering parameters (such as thrust power) and the surficial erosion or ejection is ambiguous. In addition, the measured data on flight-scale PSI (data from real missions) is insufficient to provide a reference for future landing missions (Korzun, 2021).

Because of the negative conditions mentioned, the erosion mechanisms of PSI have always been the research focus of scholars (Metzger et al., 2009a b; Sengupta et al., 2009). During the era of the Apollo missions, three typical erosion mechanisms were presented from the perspective of theoretical prediction, based on data transferred by the landing rovers. The first was viscous

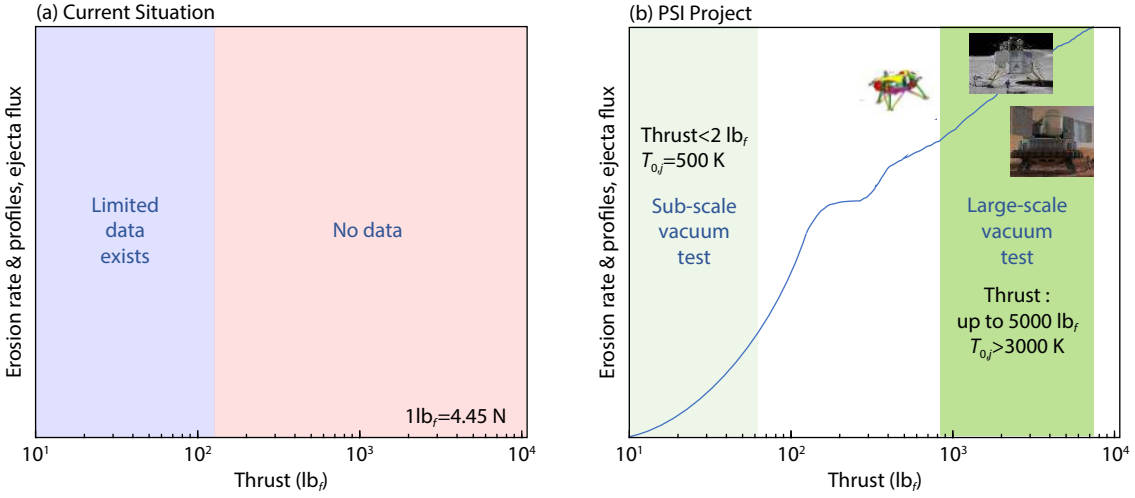

Figure 9. Schematic of the current situation of plume–surface interaction (PSI) research. (a) Current situation; (b) PSI project. $T_{0,j}$, experimental temperature; thrust: thrust of engines, 1 lb$_f$ = 4.45 N. Modified from Korzun (2021).

erosion, in which the top layer of grains is swept away by the shear stress of a wall jet (Bagnold, 2012). The second was a bearing capacity failure, in which the bulk shearing of the soil forms a cup beneath the stagnation pressure of a perpendicularly impinging jet (Alexander et al., 1966), similar to cone penetration (Figure 10). The third was diffused gas eruption, in which an auxiliary effect occurs when the stagnation pressure drives gas into the pores of the soil only to erupt, carrying soil with it at another location or time (Scott and KO, 1968). With further research and observation, another mechanism, diffusion-driven flow, was identified. Diffusion-driven flow occurs when the same stagnation pressure of the jet drives gas through the soil so that the drag of the gas becomes a distributed body force within the soil, causing the soil to fail and shear in bulk (Metzger et al., 2009a).

In addition, the interaction between the jet from the Viking lander's nonpulsed engines (thrust: 2,230 N) and the Martian soil caused only modest surface erosion (Shorthill et al., 1976a, b).

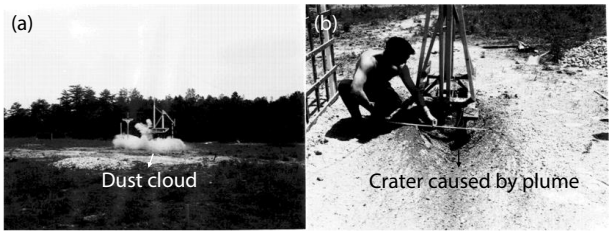

Figure 10. Plume–surface interaction terrestrial tests. (a) Experimental process; (b) *in situ* measurement. Modified from Alexander et al. (1966).

However, the lesser total thrust of the Phoenix's 12 engines, pulsating at 10 Hz with an average impingement pressure of 1/10 of the Earth's sea level pressure (Rennó et al., 2009), led to more extensive erosion on the Martian surface and even exposed the subsurface ice under the landing platform over a radius of 75 to 85 cm (Smith et al., 2009). Mehta et al. (2011) proposed a new erosion mechanism, diffusive gas explosive erosion (DGEE), based on an analysis of the Phoenix's landing process. The supersonic pulsed jets impinge on soils and generate high-pressure gradient forces to soil weight ratios. The erosion process of the Phoenix landing was dominated by DGEE. The explosive erosion during the process was induced by local liquefaction of the soil and a shock wave of annular radiation particles. The DGEE was 5–20 times larger than previous erosion mechanisms.

Nevertheless, the descriptions of erosion mechanisms mentioned are based on theoretical predictions and may not be verified by physical models. Further research involving quantitative physical models with different erosion mechanisms is needed (Figure 11).

3.2 Terrestrial Tests

Plume–surface interaction involves complicated physical coupling processes encompassing fluid mechanics, rarefied gas dynamics, soil mechanics, and a series of physical and chemical evolutions. The phenomena of PSI during planetary flight missions last several minutes and are recorded only by the cameras on the lander platforms. These directly observed images or videos of PSI can be analyzed by photogrammetry to obtain the basic information on PSI during the landing process. Detailed PSI data, such as the soil erosion rate and the particle transport condition, are

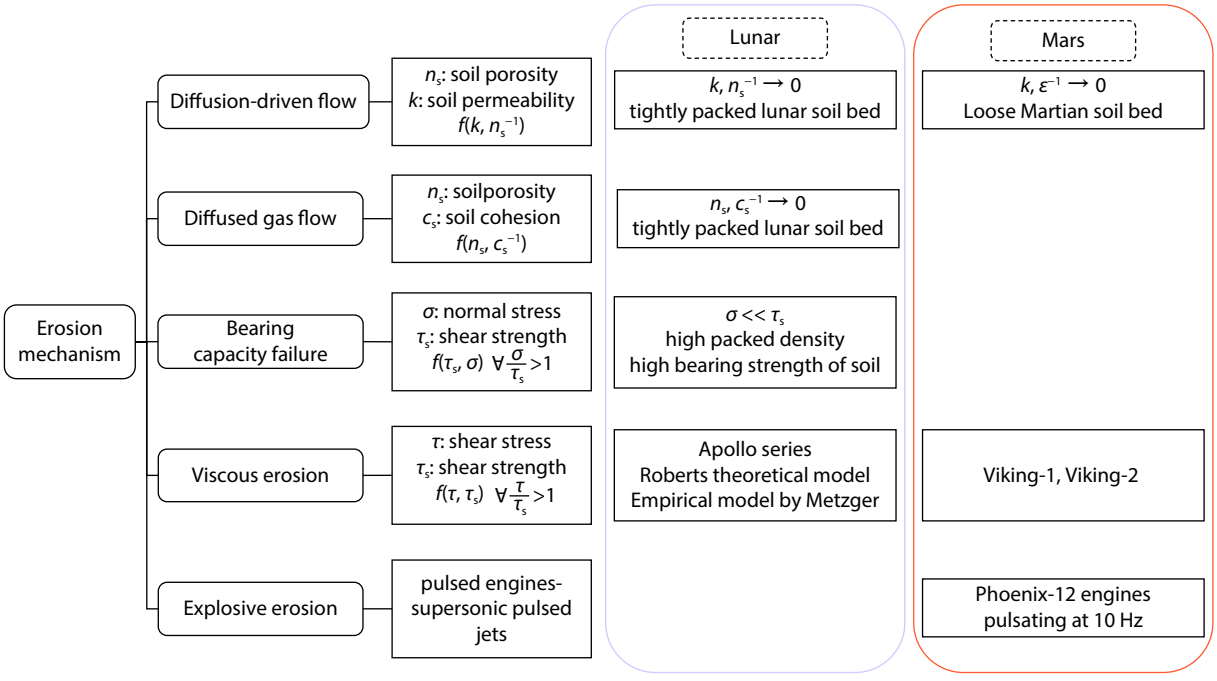

Figure 11. Erosion mechanisms of landing on Mars and the Moon. *Diffusion-driven flow* is inversely proportional to soil porosity n_s and is proportional to soil permeability k. *Diffused gas flow* is proportional to soil porosity n_s and is inversely proportional to soil cohesion c_s. A *bearing capacity failure* occurs when the normal stress σ exceeds the shear strength τ_s. *Viscous erosion* occurs when the shear stress τ exceeds the shear strength τ_s (the main erosion mechanism of the Apollo series and the Viking series). *Explosive erosion* occurs as a result of the pulsed engines (Phoenix: 12 engines pulsating at 10 Hz). Modified from Metzger et al. (2009a), Mehta et al. (2011), and Rahimi et al. (2020).

unable to be obtained directly because of the limitations of the payloads.

To study the PSI erosion law and potential risks, a series of PSI terrestrial tests have been completed under special laboratory conditions in the last century (Roberts, 1963; Land and Clark, 1965; Alexander et al., 1966; Christensen et al., 1968; Hutton, 1968). The focus of the PSI terrestrial tests includes the conditions under which particles are raised aloft, the evolution of the planetary surface, the potential pollution, and the risks of safe landings. In this section, we review previous experiments aimed at exploring PSI mechanisms.

In the 1960s, researchers built experimental platforms to study PSI during the era of planetary exploration. Early on, the PSI experiments were carried out under the Earth's environment. Scott and Ko (1968) analyzed the process of PSI and concluded that soil movement was mainly induced by the gas pressure in the soil. Christensen et al. (1968) took the images transferred from Surveyor V as benchmark media and established a consolidated soil model based on the observation data. Further experiments were then carried out based on the aforementioned model. To simulate the planetary conditions on the Moon or Mars, the vacuum condition was considered further. Mason and Nordmeyer (1969) utilized a vacuum sphere to carry out several trials on the engine height, nozzle diameter, and thrust level (Figure 12). An empirically derived erosion law was obtained based on their results, which suggested that the erosion volume was proportional to the thrust level and inversely proportional to the square root of the engine height. On the basis of the obtained erosion law, the authors predicted the erosion volume and cratering depth during the Surveyor V landing. Clark et al. (1970b) used the same vacuum sphere to simulate the Viking lander during the landing process.

Hutton et al. (1980) comprehensively analyzed the earth PSI experimental data and the observation data during the Viking-1 and Viking-2 flight missions. The results indicated no essential difference between the aforementioned two PSI processes under Earth and Mars conditions. Rajaratnam (1982) introduced a dimensionless erosion parameter E_c based on the Froude number (Fr) to forecast the scale of the final crater geometry:

$$Fr = \frac{\rho_g V^2}{\left(\rho_s - \rho_g\right) d}. \tag{3}$$

Parameter E_c gives an estimate of the ratio of the force exerted by the circular jet on a bed particle located directly under the jet and at the original bed level to its resistive force (Equation (4)):

$$E_c = \sqrt{Fr} \times \frac{D}{H}. \tag{4}$$

The two parameters above are defined by the gas velocity V, gas density ρ_g (kg/m^3), sand density ρ_s (kg/m^3), sand particle diameter d (m), nozzle height H (m), and nozzle diameter D (m) (Beltaos and Rajaratnam, 1977; Rajaratnam, 1982; Aderibigbe and Rajaratnam, 1996).

Haehnel et al. (2008) considered the issue that the erosion parameter E_c approaches infinity when the nozzle is infinitely close to the ground. Hence, the nozzle height H was displaced by the sum of the nozzle height and nozzle diameter ($H + D$):

$$E_c = \sqrt{Fr} \times \frac{D}{H + D}. \tag{5}$$

The jet regimes (Figure 13) could be identified by the values of the erosion parameter (E_c), including a strongly deflected jet regime I (SDJR I), a strongly deflected regime II (SDJR II), a weakly deflected jet regime I (WDJR I), and a weakly deflected jet regime II (WDJR II), respectively (Aderibigbe and Rajaratnam, 1996). The four jet regimes represent four stages of erosion conditions during landing operations.

After the optimization of the erosion parameter form, Haehnel et al. (2008) put forward a novel method of quantifying the interaction between the impinged jet and the loose-particle beds to obtain more effective data. They introduced a Reynolds number (Equation (6)) based on bed permeability and focused on the effect of permeability of the experimental material on cratering conditions:

$$Re_\kappa = \frac{U_s \sqrt{\kappa}}{\nu}, \tag{6}$$

where U_s is an estimate of the surface velocity based on momentum considerations for axisymmetric jets (m/s). ν is the kinematic viscosity of the fluid (Pa·s).

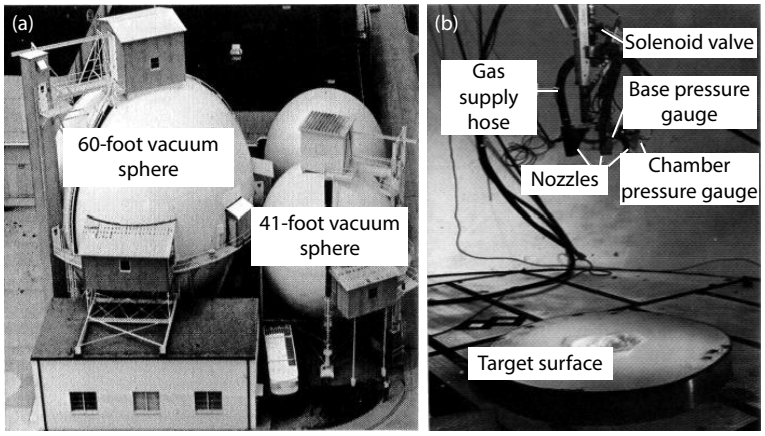

Figure 12. Schematic of the vacuum sphere experimental apparatus. (a) Vacuum sphere; (b) Apparatus inside the jet. Modified from Clark (1970b).

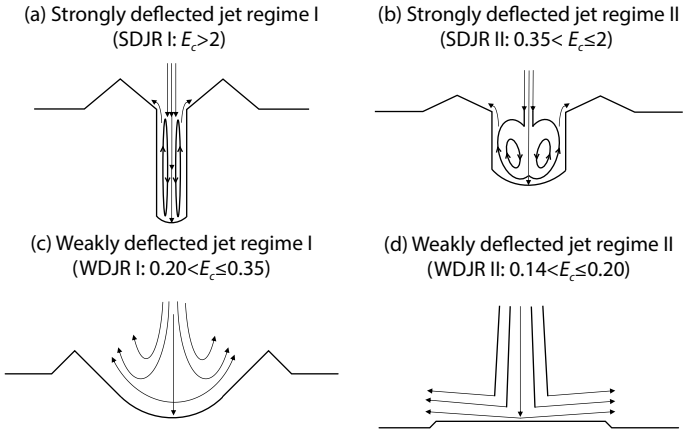

Figure 13. Sketches of flow regimes. Modified from Aderibigbe and Rajaratnam (1996).

The results showed that the equilibrium crater depth is weakly affected by the permeability of the bed material. Additionally, they provided an empirical means of calculating the maximum crater slopes (Equation (7)):

$$\frac{D_{\text{crater}}}{H} = B\left(\frac{E_c}{Re_\kappa^n}\right)^m, \tag{7}$$

where B and m are fitted parameters and empirically determined. n is also a modified exponent (n = 0.06).

A functional relationship exists between the formation rate of craters and the jet intensity (Equation (8)):

$$\frac{\mathrm{d}D_{\text{crater}}}{\mathrm{d}t} = C\frac{\rho}{\rho_\text{b}}\frac{1}{g}\left(C'\frac{U_j d}{[h+H(t)]Re_\kappa^p} - u_{*t}^2\right), \tag{8}$$

where U_j is the jet exit velocity (m/s), g is gravitational acceleration (m/s^2), ρ_b is the density of bed material (kg/m^3), and ρ is the density of fluid (kg/m^3), D_{crater} is the depth of craters (m), H is the nozzle height (m), κ is the permeability of bed material (m^2), u_{*t} is the threshold friction velocity related to the critical shear stress (m/s), p is an exponent to scale the effect of permeability on the friction velocity, and C is a constant of proportionality (s^{-1}). In addition, C' is an empirically determined scaling constant to allow the term in parentheses to go to zero when the strength of the flow drops below the threshold condition.

Donohue et al. (2005) carried out further experiments to study the relationships between the cratering rate of erosion and the gas density ρ_g/gas velocity V. An erosion function with two empirical coefficients (a, b) needed to calibrate was established to obtain the detailed cratering rate (Equation (9)):

$$d/a = \log\left\{b\left(t+\frac{1}{b}\right)\right\} \quad t \geqslant 0, \tag{9}$$

$$d/a = b\mathrm{e}^{-d/a}, \tag{10}$$

where d is the depth of crater (cm), t is time (s), e is natural constant.

The authors utilized the experimental data to fit the form of the function above. The relationships between a and b with $\rho_\text{g}V^2$ were then fitted (Equation (10)). The fitted results suggested that a is constant with the evolution of $\rho_\text{g}V^2$ (a = 0.458) and that a positive linear relationship exists between b and $\rho_\text{g}V^2$ (Equation (11); Donahue et al., 2012):

$$b = (0.00112)\,p_\text{g}V^2. \tag{11}$$

The unit of 0.00112 is $\frac{1\cdot\mathrm{s}}{\mathrm{g}\cdot\mathrm{m}}$. Researchers from NASA and the University of Michigan took Phoenix as an object and conducted a subscale cold gas thruster test to simulate the impinged dynamic involving a pulsed supersonic plume and the ground under Martian atmospheric pressure. They concluded, based on the results, that the impingement of the pulsed jet could result in soil liquefaction and gas–soil bursting. Notably, the above phenomena led to more dusty and intensive lateral erosion. The related results provided the Phoenix team with support and a reference (Mehta et al., 2007, 2008; Plemmons et al., 2008). Using the same experiment apparatus, Mehta et al. (2010) utilized a 25% scale Viking lander engine and a representative Mars simulant soil-media test bed to conduct plume impingement ground interaction experiments (Figure 14). The results showed that the primary erosion mechanism was soil bulk shear failure and the nonlinear dependence of erosion on the thrust level, ground slope, and particle size. Another critical conclusion was that supersonic jets at the atmospheric pressure of Mars (underexpanded) produced a greater erosion rate than did jets (highly overexpanded) at the atmospheric pressure of Earth.

With the aim of examining lunar and Martian plume effects, the team from NASA's Kennedy Space Center conducted a series of PSI simulation experiments. The erosion mechanism and the cali-

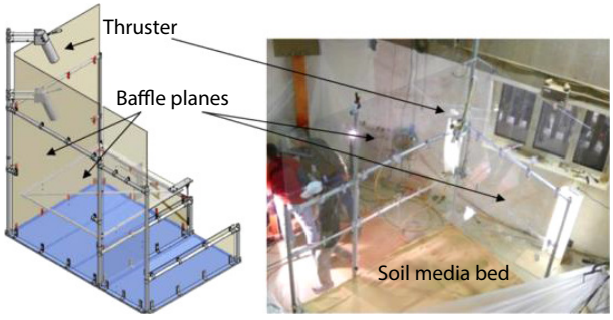

Figure 14. Experimental apparatus used by Mehta et al. (2010) to study plume–surface interaction.

bration relationship were described in detail, and the authors proposed a new diffusion-driven flow mechanism, which had been ignored during the era of Apollo and Viking (Metzger et al., 2009a, b, c). The researchers from NASA's Jet Propulsion Laboratory carried out PSI experiments aimed at using the new sky crane landing mode in advance of the MSL mission. By quantifying the erosion conditions, this program provided insights into landing site selection, rover operational constraints, and the throttle level profile during touchdown and fly-away (Sengupta et al., 2009).

In addition to the planetary atmospheric conditions, the soil material is also a key interest. A series of lunar and Martian simulants were formulated for different purposes, such as to test the mechanics and components of the soil. Surficial media such as real Martian or lunar regolith are beneficial for conducting PSI simulation experiments. Clegg et al. (2011) utilized simulant JSC-1A to study the soil erosion mechanisms during the process of landing on the lunar surface. Metzger et al. (2011) chose the Mauna Kea lunar testing site in Hawaii to conduct *in situ* PSI ground experiments. The results were analyzed and combined with the Apollo descent and ascent videos and terrestrial images. Immer and Metzger (2010) conducted three PSI case studies under Martian and lunar atmospheric conditions: the Handheld Observation of Scour Holes (HOOSH), Handheld Angle of Repose Measurements of Lunar Simulants (HARMLuS), and Mars Architecture Team study (MATS). The HOOSH was conducted to survey the functions of cratering and gravity level (Mars, Moon). The HARMLuS aimed to measure the failure angle related to the angle of repose under Martian and lunar gravity. The MATS aimed to study the effect of soil consolidation on the particle cratering mechanism.

The results of the experiments above suggested that the lower gravity resulted in more intensive cratering and a larger failure angle. In addition, the increased consolidation of lunar simulants resulted in a larger failure angle. Guleria and Patil (2020) utilized glass bead particle materials to conduct a jet impact cratering experiment. Through analysis of the experimental results, they found a positive linear relationship between the stable depth of the crater and the jet flow rate. They found that under the conditions of a given jet flow rate, a logarithmic relationship exists between the depth of the impact crater and time. Chambers et al. (2021) used the gas–regolith interaction testbed to conduct a PSI drop tower experiment at the Kennedy Space Center for microgravity research (Figure 15). Four different media were utilized: steel beads, quartz sand, glass beads, and a high-fidelity asteroid regolith simulant. They concluded that a trend exists of PSI behaviors being significantly more conspicuous at reduced gravity. A key conclusion was that viscous shear erosion appears to be the dominant mechanism for PSI in fine-grained, low-permeability media, whereas diffusion-driven flow appears to be dominant in large-grained, high-permeability media, and bearing capacity failure could be observed in intermediate-sized particles between these two regimes. At the same time, Kuhns et al. (2021) conducted cratering scale experiments during the lunar landing, including drop tower testing and terrestrial conditions testing (Figure 16). They obtained parts of the basic data, and their experiments have provided support for future lunar landing missions.

According to the previous reviews, terrestrial PSI simulation experiments are challenged by four main difficulties. First, the proper planetary regolith simulants are difficult to prepare because of the material types, particle size, particle gradation, particle rounding, and particle cementation. Second, establishing

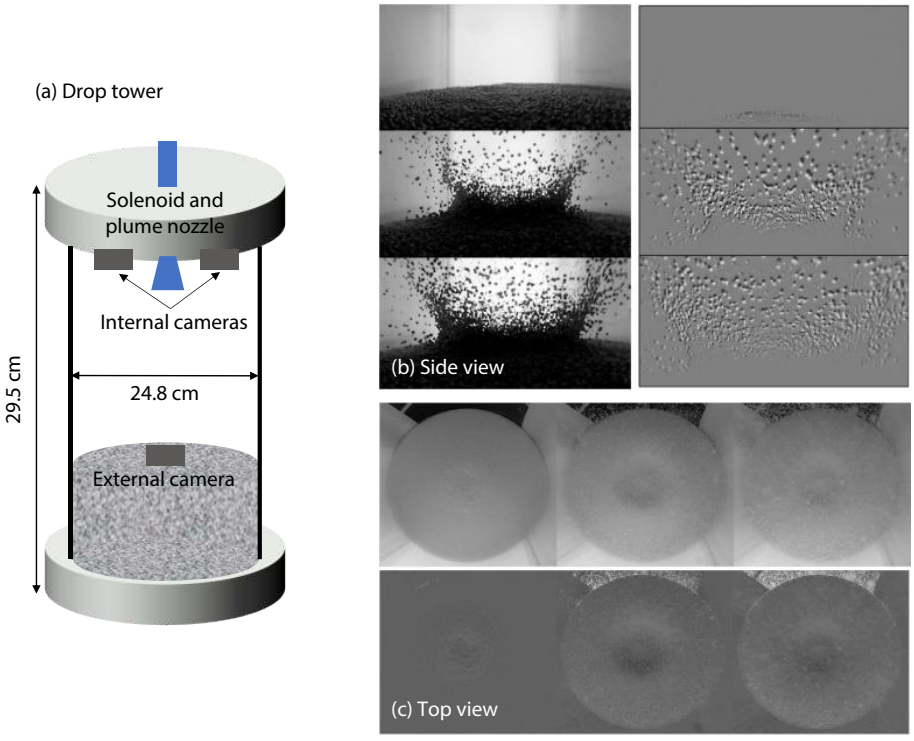

Figure 15. Drop tower apparatus. (a) Schematic of a drop tower; (b) Images of the side view; (c) Images of the top view. Modified from Kuhns et al. (2021).

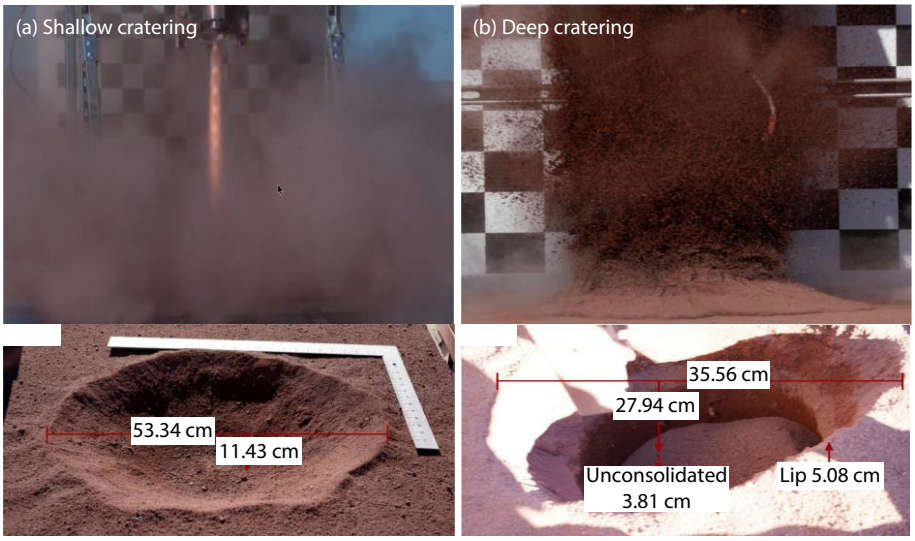

Figure 16. Hot fire results. (a) Shallow cratering; (b) Deep cratering. Modified from Kuhns et al. (2021).

similar planetary environments (e.g., atmospheric conditions, temperature, low gravity) is challenging. Third, recording the quantitative data (e.g., changes in the planetary surface, particle transport) is another knowledge gap for PSI experiments. Fourth, the lander-scale engines are difficult to deploy in terrestrial tests. Terrestrial PSI tests should focus on the construction of similar planetary conditions and flight-scale simulations. More specific contents are discussed in the next section.

4. Challenges and Prospects

4.1 The Lack of Complete Data on PSI Process Monitoring

Plume–surface interaction data consist of the resulting data from full-scale landing operations and terrestrial tests of PSI. The former include engineering data (nozzle heights, nozzle thrusts, plume temperature, flight attitudes) and image data (images, videos) recorded during the landing process. Given the limitation of payloads on the landing platforms, critical data on PSI, such as the temperature and velocity of high-speed gas, the erosion volume, the erosion rate, and movement of the soil, are difficult to obtain because of the lack of payloads designed for PSI research. In the future, specially designed payloads for collecting PSI data will provide a critical foundation for PSI research.

Another part of the PSI data was obtained from terrestrial tests. Currently, the geometry of craters and the erosion mass/rate are the main objects recorded during a PSI experiment. Other related data have not been recorded well during the experiments, such as the temperature of soil particles and gas, structural changes, and the transport of particles. Therefore, a novel test system recording more dynamic information on PSI is desperately needed.

4.2 The Challenges of Terrestrial Tests

Research on terrestrial tests of PSI has mainly focused on the clarity of erosion mechanisms and the erosion scale law. According to previous reviews of the evolution of PSI in terrestrial tests, the challenges of terrestrial tests consist of three key aspects:

(1) The phenomena of PSI are mainly controlled by the test soil bed (Table 4), which includes the soil materials and the soil structure (i.e., cohesion, internal friction angle). Hence, the most important direct factor in the PSI process is the soil media. As described previously, the Heat Flow and Physical Properties Package (HP^3) carried by InSight has not achieved the set goals of implementing a vertical string of temperature sensors in the soil to a depth of 5 m, then measuring the surface heat flow because of the lack of knowledge of Martian soil (Spohn et al., 2022a, b). Currently, some planetary soil simulants (Taylor et al., 2016; Alexiadis et al., 2017; Oravec et al., 2021) are designed based on different motivations, including to determine the spectrum properties (JC Mars-1, MGS-1, JMSS-1), astrobiology (P-MRS, S-MRS), *in situ* resource utilization (UC Mars 1, MGS-1C), and engineering (MMS, SSC, ES-X, MER). However, some key issues still exist in the work on soil simulants. Reference to the deep profile data of Martian soil and lunar soil is lacking, and the soil simulants designed for terrestrial tests are not being completed from the perspective of their mechanical properties. In addition, the technology used to prepare the soil simulants needs to be further improved.

(2) Such complicated experimental platforms are difficult to establish because of their vacuum, low pressure, and low gravity. Researchers aiming to achieve this goal have adopted a vacuum apparatus to simulate the lunar conditions (Clark, 1970b) and have used a drop tower to simulate the low gravity (Kuhns et al., 2021). However, the vacuum sphere and drop tower are necessarily limited in size. The size of the apparatus is commonly enlarged by

Table 4. Typical planetary regolith simulants.

Simulant	Name	Note	Simulant	Name	Note
Moon	JCS-1A	USA	Mars	JSC Mars-1	USA
	MLS-1			MMS	
	CAS-1	China		ES-1/2/3	UK
	CUG-1A			DLR-A/B	German
	TJ-1			JLU Mars 1/2/3	China
	JLU			TJ-M1	

increasing the manufacturing cost. For low gravity, three common simulation methods exist: the direct simulation method, the force equilibrium method, and the similarity simulation method. Among the three methods, the force equilibrium method consists of two parts: the vertical equilibrium and the diagonal equilibrium. The similarity simulation method is a similarity criterion used with dimensional analyses to simulate the physical phenomena that accompany low gravity. However, a huge gap exists when reconstructing a real planetary environment like that on Mars or the Moon.

(3) Another critical factor in determining the PSI is the plume from the thrust engine (Figure 17). The plume from the thrust engine directly influences the PSI phenomenon by affecting the erosion mechanism and erosion rate. The phenomena of PSI are dominated by the designs and configurations of the descent engines. The configuration of the engines must be verified before the missions can be implemented (Romine et al., 1973). To obtain reliable data on PSI, the real thrust engines to be used on the landing platforms are the best choice for implementing terrestrial tests.

Research on PSI will be further improved by considering the three problems mentioned to some extent, which can provide a better reference for the planetary exploration plans and a greater possibility of achieving the scientific goals.

4.3 Prospects of PSI

The phenomena of PSI include surficial erosion, cratering, blowing rocks, pits on the lunar surficial media, and pits on the surrounding apparatus. The aforementioned phenomena are common during exploration landing operations. Initially, the motivations for the PSI study were to ensure a safe landing and to avoid the risk of damaging the apparatus. Although the PSI creates many challenges for landing missions, it provides the opportunity to study the planetary soil properties and shallow structure directly. The PSI can provide new insights into planetary science in at least the following two ways:

(1) The erosion and cratering of PSI can directly reveal the shallow structures of Mars or the Moon. The photographs and videos transferred from the payloads on the landing platforms contain specific shallow stratigraphic profile information, including the shape, color, size, and cementation of particles. For example, the landing crater of Phoenix directly exposed the subsurface ice. Other scientific data on payloads also provide information on the materials and structures. Taking the Zhurong rover as an example, the Mars Surface Composition Detector (MarSCoDe) can detect Martian rock and soil targets of interest. By combining the techniques of active laser-induced breakdown spectroscopy, passive short-wave infrared, and micro-imaging, MarSCoDe provides the functions of elemental composition discrimination and quantitative determination, the classification of rock and soil characteristics, the imaging of sample texture, and the characterization of the plasma-excited area (Xu MW et al., 2021). The Mars Rover Penetrating Radar (RoPeR) can penetrate the surface and constrain stratigraphic structures of a specific depth range,

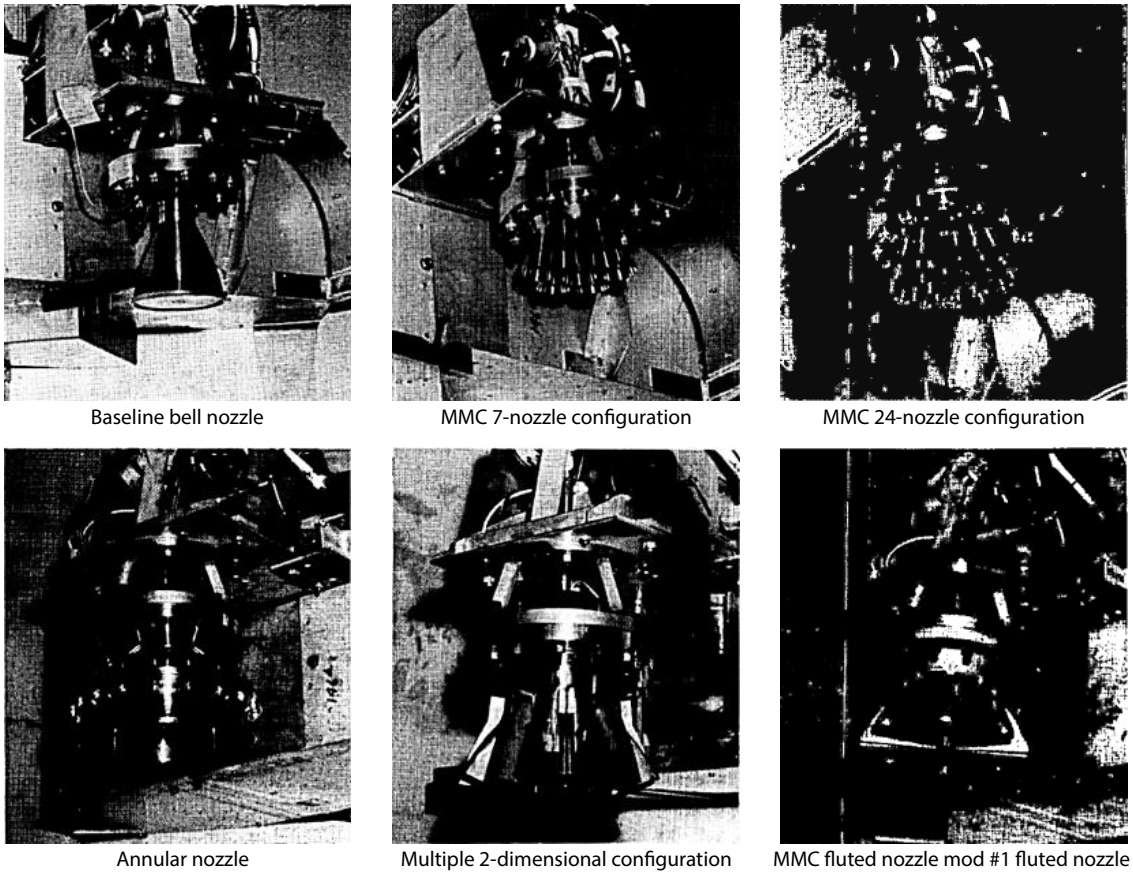

Figure 17. Nozzle configurations and design. Modified from Romine et al. (1973), contrast adjusted.

depending on the frequency band (i.e., high-frequency channels of ~1 to several meters, and the low-frequency channels of 10–80 m, Li C et al., 2022). The PSI exposed the subface directly, which can provide information on the depth range gap (~0–0.5 m) without extra operations such as drilling. Therefore, joint detection at different scales (MarSCoDe–PSI–RoPeR) could provide a comprehensive interpretation of the Martian structure and help establish a multiscale profile to identify its composition and structures (Figure 18).

Using the image data from the Zhurong rover, we conducted preliminary research on PSI to add basic information on the depth of 0–0.4 m based on the camera images and our photogrammetry reconstruction work (Figure 19). The plume of Tianwen-1 created a landing crater with a depth of > 40 cm and a diameter of ~1.2 m, which is the deepest landing crater on a planetary surface reported to date. As shown by the textures, sizes, and colors of the soil, it exposed a stratigraphic layering structure in the subsurface (Figure 19a) that was vaguely revealed inside the landing crater, potentially indicating the different layers and mineral compositions. Columnar-like rock blocks could be found at the bottom of the landing crater, which we assumed to be *in situ* rock. We used binocular matching data, calculated according to the 3-D coordinates of the top and bottom feature points of the rock, by using the forward intersection method, and we constrained the height of the rock by at least 15 cm. Wu B et al. (2022) and Ding L et al. (2022) reconstructed a digital elevation model (DEM) of the landing site and reported the depth of the crater to be > 24 cm, with reference to the top of the column at the bottom of the landing crater. Further study of the Tianwen-1 landing crater (layering structures and mineral compositions) will be conducted in the future.

(2) The craters caused by the erosion of PSI could provide more information on the mechanical properties of planetary soil. A miniature free slope surface was formed by the PSI process, and the slope stability analysis could be utilized to limit the soil mechanical properties, such as the internal friction angle and cohesion (Golombek et al., 2020). The common routine is to utilize the limit equilibrium method to analyze the soil slope stability by using the Culmann method or the Morgenstern–Price method. This calculation could provide a reliable lower limit of the mechanical properties of soil. The forward intersection algorithm using the dense matching points of binocular vision allows the acquisition of 3-D point cloud coordinates for DEM reconstruction.

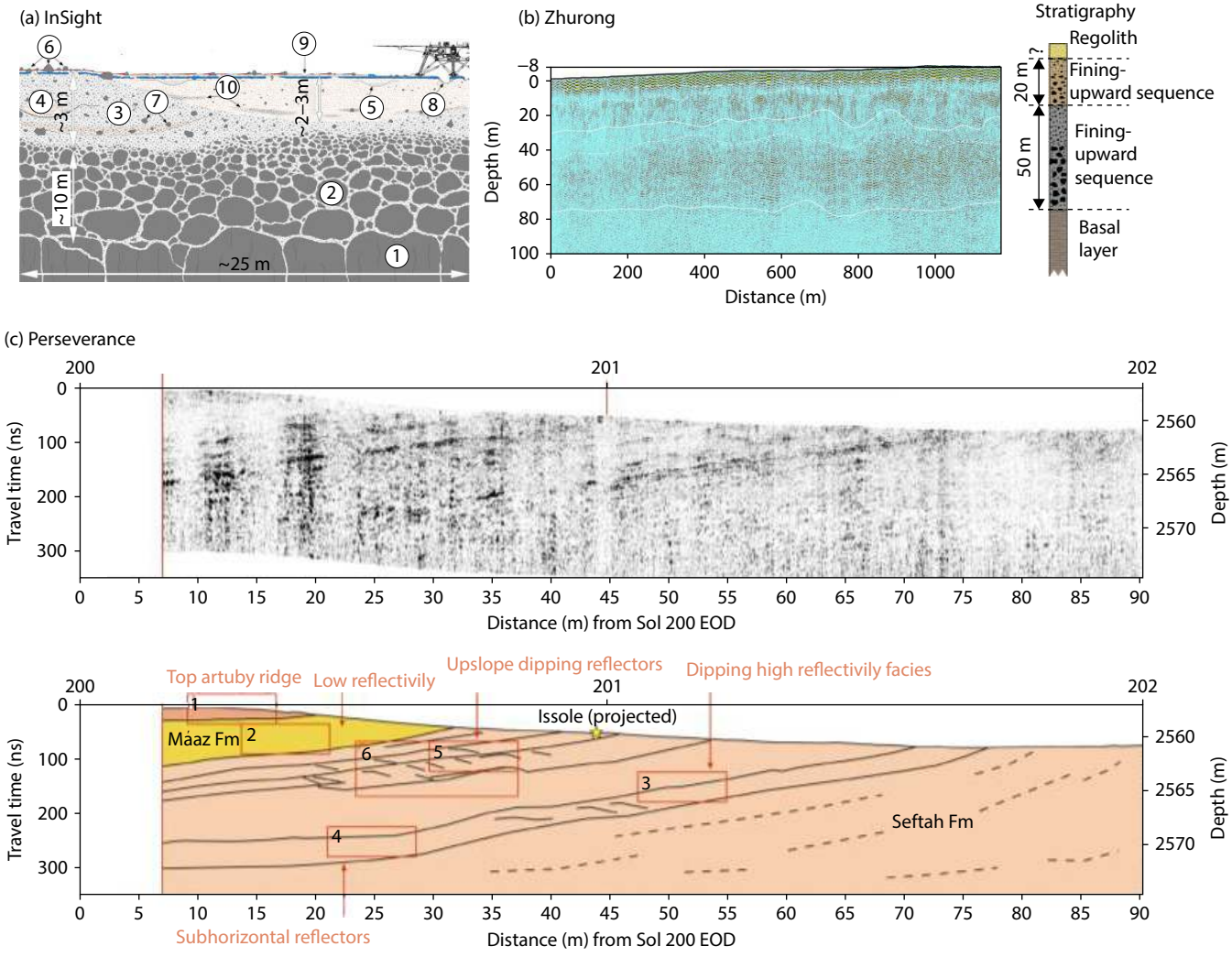

Figure 18. Interpretive cross section of the subsurface on Mars. (a) InSight; (b) Zhurong; (c) Perseverance (Golombek et al., 2020; Hamran et al., 2022; Li C et al., 2022).

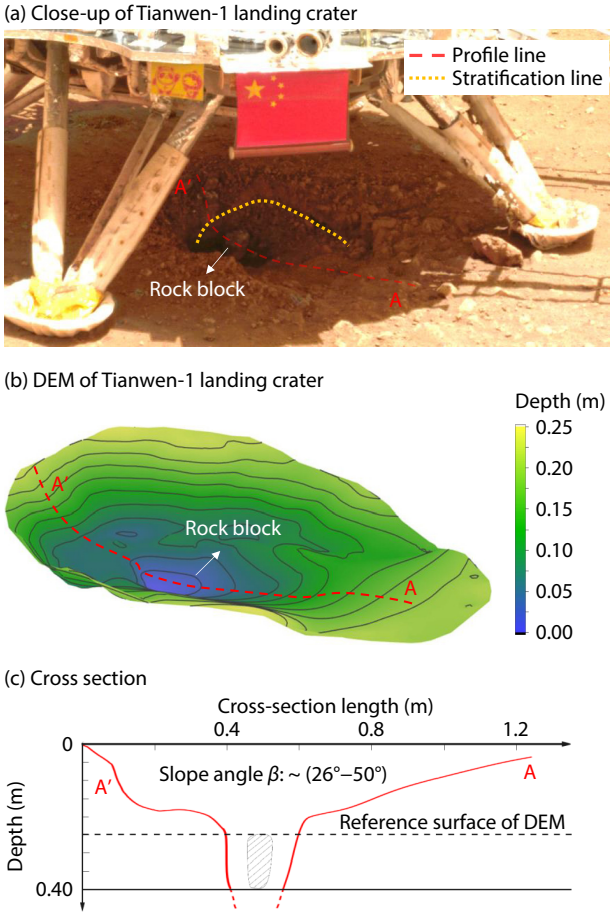

Figure 19. Close-up and digital elevation model (DEM) near the Tianwen-1 landing crater and a cross section of the depth. (a) Close-up near the Tianwen-1 landing crater. Note the columnar-like rock block at the bottom of the landing crater (height: ~15 cm). Base image from the China National Space Administration, contrast adjusted. (b) DEM of the landing crater and the nearby terrain surface generated from photogrammetric processing of stereo pairs of Navigation and Terrain Cameras (NaTeCams) images (3-D view: The angle is roughly consistent with (a)). The deepest location of the DEM is close to the top of the columnar-like rock block. The red line represents the cross section of A–A′. The black dashed line represents the reference surface of the DEM. (c) A representative cross section of the landing crater (A–A′).

The navigation terrain camera used to capture the Zhurong landing crater was positioned 6 m away. The accuracy of the DEM reconstruction decreased as the distance between the camera and the object being photographed increased. As a result, by using feature point measurement on the Zhurong lander, the DEM could achieve an accuracy of within 10% in the vicinity of the landing crater. From the DEM with the 3-D view of the landing crater and the nearby terrain surface (Figure 19b), a representative cross section of depth (A–A′) with a steep slope was selected, and the slope angle was estimated to be in the range of ~26°–50° (Figure 19c). Further, the low-limit mechanical properties of Martian soil were obtained by the Morgenstern–Price method based on the slope geometry of the cross section (Zhu DY et al., 2005). It was concluded that the low-limit cohesion range was 90–130 Pa when the internal friction angle was in the range of 21°–34°. The analysis of landing craters can provide further restriction of soil properties and support future missions, including sampling and base construction.

The initial motivation for PSI research was ensuring safe landings for the missions because of the unsolved major risk of propulsive landing. Advances in past and ongoing planetary exploration have proved that investigation of the PSI potentially provides opportunities to obtain new insights into planetary science. We urge further research to develop an integrated modeling, simulation, and testing approach to PSI, to take advantage of PSI phenomenology and data to explore the environmental and subsurface information of the planet, such as the erosion physics, composition, and mechanical properties of the soil. Given that landing craters can directly expose the subsurface structures and materials without additional complicated operations, we suggest that the first detection target of payloads can be set to landing craters at the initial stage of missions. Before the movement of rovers, more effective data on the planetary subsurface can be obtained near landing sites with little risk. Critical data from the surface to the subsurface at landing sites, including the spectrum, mineral components, structures, and thermal properties, can be used in combination with other detection methods to obtain unknown attributes of the shallow layer (approximately <0.5 m) and establish a comprehensive understanding of Mars.

Acknowledgments

We thank all the scientists and engineers who were involved in the Tianwen-1 mission, including the CNSA, the National Astronomical Observatories of the Chinese Academy of Sciences (NAOC), China Academy of Space Technology (CAST), Beijing Aerospace Control Center (BACC), and other critical institutes. The scientific data were provided by CNSA and the State Administration of Science Technology and Industry for National Defense. We also appreciate the instruction and discussions on photogrammetry, engineering and engine data, and Martian composition from Geng Yan, Dong Jie, Lin Yangting, Qin Xiaoguang, Zhang Jinhai, Du Aimin, Di Kaichang, Wan Wenhui, Liu Shaochuang, Zhang Zhigang, Yue Zongyu, Liu Yike, Ren Xin, Gou Sheng, Zhang Shuo, Xu Changyi, Chai Lihui, Guo Guangjun, Zhang Lei, Ye Qing, Xiao Zhuowei, Maryelin Josefina Briceño, Guo Jingyun, and other experts supporting our work. In addition, we appreciate the support from Wu Fuyuan and Pan Yongxin, leaders of the Mars Mission at the Institute of Geology and Geophysics, Chinese Academy of Sciences (CAS). This work was supported by the National Natural Science Foundation of China (Grant 42230111), the Key Research Program of the Institute of Geology and Geophysics, CAS (Mars Mission; Grant IGGCAS-202102), the Key Research Program of the Institute of Geology and Geophysics, CAS (Grant IGGCAS-201904), and the CAS Key Technology Talent Program.

The authors declare they have no known competing financial interests or personal relationships that could have appeared to influence the work reported in this paper.

References

Aderibigbe, O. O., and Rajaratnam, N. (1996). Erosion of loose beds by

submerged circular impinging vertical turbulent jets. *J. Hydraul. Res.*, *34*(1), 19–33. https://doi.org/10.1080/00221689609498762

Alexander, J. D., Roberds, W. M., and Scott, R. F. (1966). *Soil Erosion by Landing Rockets Final Report*. Houston: Manned Spacecraft Center.

Alexiadis, A., Alberini, F., and Meyer, M. E. (2017). Geopolymers from lunar and Martian soil simulants. *Adv. Space Res.*, *59*(1), 490–495. https://doi.org/10.1016/j.asr.2016.10.003

Arvidson, R. E., Anderson, R. C., Bartlett, P., Bell III, J. F., Blaney, D., Christensen, P. R., Chu, P., Crumpler, L., Davis, K., … Wilson, J. (2004a). Localization and physical properties experiments conducted by Spirit at Gusev Crater. *Science*, *305*(5685), 821–824. https://doi.org/10.1126/science.1099922

Arvidson, R. E., Anderson, R. C., Bartlett, P., Bell III, J. F., Christensen, P. R., Chu, P., Davis, K., Ehlmann, B. L., Golombek, M. P., … Wilson, J. (2004b). Localization and physical property experiments conducted by opportunity at meridiani planum. *Science*, *306*(5702), 1730–1733. https://doi.org/10.1126/science.1104211

Arvidson, R. E., Squyres, S. W., Anderson, R. C., Bell III, J. F., Blaney, D., Brückner, J., Cabrol, N. A., Calvin, W. M., Carr, M. H., … Yen, A. (2006). Overview of the spirit mars exploration rover mission to Gusev Crater: landing site to backstay rock in the Columbia hills. *J. Geophys. Res.*: *Planets*, *111*(E2), E02S01. https://doi.org/10.1029/2005JE002499

Arvidson, R. E., Bellutta, P., Calef, F., Fraeman, A. A., Garvin, J. B., Gasnault, O., Grant, J. A., Grotzinger, J. P., Hamilton, V. E., … Wiens, R. C. (2014). Terrain physical properties derived from orbital data and the first 360 sols of Mars Science Laboratory Curiosity rover observations in Gale Crater. *J. Geophys. Res.*: *Planets*, *119*(6), 1322–1344. https://doi.org/10.1002/2013je004605

Bagnold, R. A. (2012). *The Physics of Blown Sand and Desert Dunes*. Mineola, New York: Courier Corporation.

Banerdt, W. B., Smrekar, S. E., Banfield, D., Giardini, D., Golombek, M., Johnson, C. L., Lognonné, P., Spiga, A., Spohn, T., … Wieczorek, M. (2020). Initial results from the InSight mission on Mars. *Nat. Geosci.*, *13*(3), 183–189. https://doi.org/10.1038/s41561-020-0544-y

Beltaos, S., and Rajaratnam, N. (1977). Impingement of axisymmetric developing jets. *J. Hydraul. Res.*, *15*(4), 311–326. https://doi.org/10.1080/00221687709499637

Braun, R. D., and Manning, R. M. (2007). Mars exploration entry, descent, and landing challenges. *J. Spacecr. Rockets*, *44*(2), 310–323. https://doi.org/10.2514/1.25116

Bridges, J. C., Clemmet, J., Croon, M., Sims, M. R., Pullan, D., Muller, J. P., Tao, Y., Xiong, S., Putri, A. R., … Pillinger, J. M. (2017). Identification of the Beagle 2 lander on Mars. *Roy. Soc. Open Sci.*, *4*(10), 170785. https://doi.org/10.1098/rsos.170785

Capecelatro, J. (2022). Modeling high-speed gas-particle flows relevant to spacecraft landings. *Int. J. Multiphase Flow*, *150*, 104008. https://doi.org/10.1016/j.ijmultiphaseflow.2022.104008

Chambers, W. A., Dove, A. R., Cox, C. T., and Metzger, P. T. (2021). Plume-surface interaction phenomena observed in vacuum microgravity. In P. J. van Susante, et al. (Eds.), *Earth and Space 2021* (pp. 22-31). American Society of Civil Engineers. https://doi.org/10.1061/9780784483374.003

Chen, J. L. (2014). The surveyor series. In J. L. Chen (Ed.), *How to Find the Apollo Landing Sites* (pp. 185-198). Cham: Springer. https://doi.org/10.1007/978-3-319-06456-7_11

Cherkasov, I. I., Kemurjian, A. L., Mikhailov, L. N., Mikheyev, V. V., Musatov, A. A., Smorodinov, M. I., and Shvarev, V. V. (1969). Investigations of the physical and mechanical properties of the moon's soil from Luna 13. In F. J. Malina (Ed.), *Research in Physics and Chemistry* (pp. 75-77, p1-p2, 77). Oxford: Pergamon. https://doi.org/10.1016/B978-0-08-013400-0.50008-6

Christensen, E. M., Batterson, S. A., Benson, H. E., Chandler, C. E., Jones, R. H., Scott, R. F., Shipley, E. N., Sperling, F. B., and Sutton, G. H. (1967a). Lunar surface mechanical properties-Surveyor. *J. Geophys. Res.*, *72*(2), 801–813. https://doi.org/10.1029/JZ072i002p00801

Christensen, E. M., Choate, R., Jaffe, L. D., Spencer, R. L., Sperling, F. B., Batterson, S. A., Benson, H. E., Hutton, R. E., Jones, R. H., … Sutton, G. H. (1967b). Surveyor V: lunar surface mechanical properties. *Science*, *158*(3801), 637–640. https://doi.org/10.1126/science.158.3801.637

Christensen, E. M., Batterson, S. A., Benson, H. E., Choate, R., Hutton, R. E., Jaffe, L. D., Jones, R. H., Ko, H. Y., Schmidt, F. N., … Sutton, G. H. (1968). Lunar surface mechanical properties. *J. Geophys. Res.*, *73*(22), 7169–7192. https://doi.org/10.1029/JB073i022p07169

Christensen, E. M. (1970). Lunar surface mechanical properties: surveyor results. *Radio Sci.*, *5*(2), 171–180. https://doi.org/10.1029/RS005i002p00171

Clark, L. V. (1970a). *Effect of Retrorocket Cant Angle on Ground Erosion-A Scaled Viking Study*. Washington: National Aeronautics and Space Administration.

Clark, L. V. (1970b). *Experimental Investigation of Close-Range Rocket-Exhaust Impingement on Surfaces in a Vacuum*. Washington: National Aeronautics and Space Administration.

Clegg, R. N., Metzger, P. T., Huff, S., and Roberson, L. B. (2011). Lunar soil erosion physics for landing rockets on the moon. In *42nd Annual Lunar and Planetary Science Conference* (pp. 1450). The Woodlands, Texas, USA.

Clegg, R. N., Jolliff, B. L., and Metzger, P. T. (2012). Photometric analysis of the Apollo landing sites. In K. Zacny, et al. (Eds.), *Earth and Space 2012* (pp. 218-227). Pasadena, California, United States: American Society of Civil Engineers. https://doi.org/10.1061/9780784412190.025

Clegg-Watkins, R. N., Jolliff, B. L., Boyd, A., Robinson, M. S., Wagner, R., Stopar, J. D., Plescia, J. B., and Speyerer, E. J. (2016). Photometric characterization of the Chang'e-3 landing site using LROC NAC images. *Icarus*, *273*, 84–95. https://doi.org/10.1016/j.icarus.2015.12.010

Costes, N. C., Carrier, W. D., Mitchell, J. K., and Scott, R. F. (1970). Apollo 11 soil mechanics investigation. *Science*, *167*(3918), 739–741. https://doi.org/10.1126/science.167.3918.739

Ding, L., Zhou, R., Yu, T., Gao, H., Yang, H., Li, J., Yuan, Y., Liu, C., Wang, J., … Di, K. (2022). Surface characteristics of the Zhurong Mars rover traverse at Utopia Planitia. *Nat. Geosci.*, *15*(3), 171–176. https://doi.org/10.1038/s41561-022-00905-6

Donahue, C. M., Metzger, P. T., and Immer, C. D. (2012). Functional scaling for the cratering of a granular surface by an impinging jet. In R. B. Malla, et al. (Eds.), *Earth & Space 2006* (pp. 1-6). Houston, Texas, United States: American Society of Civil Engineers. https://doi.org/10.1061/40830(188)20

Donohue, C. M., Metzger, P. T., and Immer, C. D. (2005). Empirical scaling laws of rocket exhaust cratering. In: 56th Intemational Astronautical Congress, October 17-21, Fukuoka, Japan. https://doi.org/10.48550/arXiv.2104.05176

Fontes, D. H., and Metzger, P. T. (2022). Rocket plume interacting with mars soil particulates. In *AIAA SCITECH 2022 Forum*. San Diego: American Institute of Aeronautics and Astronautics. https://doi.org/10.2514/6.2022-0742

Golombek, M., Warner, N. H., Grant, J. A., Hauber, E., Ansan, V., Weitz, C. M., Williams, N., Charalambous, C., Wilson, S. A., … Banerdt, W. B. (2020). Geology of the InSight landing site on Mars. *Nat. Commun.*, *11*(1), 1014. https://doi.org/10.1038/s41467-020-14679-1

Golombek, M. P. (1997). The mars pathfinder mission. *J. Geophys. Res.*: *Planets*, *102*(E2), 3953–3965. https://doi.org/10.1029/96JE02805

Guleria, S. D., and Patil, D. V. (2020). Experimental investigations of crater formation on granular bed subjected to an air-jet impingement. *Phys. Fluids*, *32*(5), 053309. https://doi.org/10.1063/5.0006613

Haehnel, R. B., Dade, W. B., and Cushman-Roisin, B. (2008). Crater evolution due to a jet impinging on a bed of loose particles. In W. K. Binienda (Ed.), *Earth & Space 2008* (pp. 1-10). Long Beach, California, United States: American Society of Civil Engineers. https://doi.org/10.1061/40988(323)2

Hamran, S. E., Paige, D. A., Allwood, A., Amundsen, H. E. F., Berger, T., Brovoll, S., Carter, L., Casademont, T. M., Damsgård, L., … Øyan, M. J. (2022). Ground penetrating radar observations of subsurface structures in the floor of Jezero crater, Mars. *Sci. Adv.*, *8*(34), eabp8564. https://doi.org/10.1126/sciadv.abp8564

Hinners, N. W., and El-Baz, F. (1972). *Surface Disturbances at the Apollo 15 Landing Site*. Washington: National Aeronautics and Space Administration.

Huang, H., Wang, X., Chen, Y., Zhang, Q., Zhao, F. Y., Ren, X., Zeng, X. G., Yan, W., Chen, W. L., … Liu, J. J. (2023). Observations and interpretations of geomorphologic features in the Tianwen-1 landing area on Mars by using orbital imagery data. *Earth Planet. Phys.*, *7*(3), 331–346. https://doi.org/10.26464/epp2023005

Hutton, R. E. (1968). *Comparison of Soil Erosion Theory with Scaled LM Jet Erosion Tests*. Redondo Beach: National Aeronautics and Space Administration.

Hutton, R. E., Moore, H. J., Scott, R. F., Shorthill, R. W., and Spitzer, C. R. (1980). Surface erosion caused on Mars from Viking descent engine plume. *Moon.*

Planets, *23*(3), 293–305. https://doi.org/10.1007/BF00902045

Immer, C., and Metzger, P. T. (2010). Rocket cratering in simulated lunar and Martian environments. In G. B. Song, et al. (Eds.), *Earth and Space 2010* (pp. 182-190). Honolulu, Hawaii, United States: American Society of Civil Engineers. https://doi.org/10.1061/41096(366)20

Immer, C., Lane, J., Metzger, P. T., and Clements, S. (2011a). Apollo video photogrammetry estimation of plume impingement effects. *Icarus*, *214*(1), 46–52. https://doi.org/10.1016/j.icarus.2011.04.018

Immer, C., Metzger, P. T., Hintze, P. E., Nick, A., and Horan, R. (2011b). Apollo 12 lunar module exhaust plume impingement on lunar surveyor III. *Icarus*, *211*(2), 1089–1102. https://doi.org/10.1016/j.icarus.2010.11.013

Johnson, S. W., and Chua, K. M. (1993). Properties and mechanics of the lunar regolith. *Appl. Mech. Rev.*, *46*(6), 285–300. https://doi.org/10.1115/1.3120358

Katzan, C. M., and Edwards, J. L. (1991). *Lunar Dust Transport and Potential Interactions with Power System Components*. Washington: National Aeronautics and Space Administration. https://doi.org/10.2172/10181067

Korzun, A. (2021). Powered descent and plume-surface interaction. In *EDL Summer Seminar Series*.

Kuhns, M., Metzger, P. T., Dove, A., Byron, J., Lamb, S., Roberson, T., Lohman, L., Chambers, W., Rixon, G., … van Susante, P. (2021). Deep regolith cratering and plume effects modeling for lunar landing sites. In P. J. van Susante, et al. (Eds.), *Earth and Space 2021* (pp. 62-78). American Society of Civil Engineers. https://doi.org/10.1061/9780784483374.007

Land, N. S., and Clark, L. V. (1965). *Experimental Investigation of Jet Impingement on Surfaces of Fine Particles in A Vacuum Environment*. Washington: National Aeronautics and Space Administration.

Lane, J. E., Metzger, P. T., Immer, C. D., and Li, X. Y. (2008). Lagrangian trajectory modeling of lunar dust particles. In W. K. Binienda (Ed.), *Earth & Space 2008* (pp. 1-9). Long Beach, California, United States: American Society of Civil Engineers. https://doi.org/10.1061/40988(323)3

Leonovich, A. K., Gromov, V. V., Rybakov, A. V., Petrov, V. K., Pavlov, P. S., Cherkasov, I. I., and Shvarev, V. V. (1971). Studies of lunar ground mechanical properties with the self-propelled Lunokhod-1. In *Pereduizhnaya Laboratoriya na Luna-Lunokhod-I* (pp. 120-135).

Leonovich, A. K., Gromov, V. V., Dmitriyev, A. D., Lozhkin, V. A., Penetrigov, V. N., Semyonov, P. S., Grannik, I. N., Grushevsky, V. P., and Shvaryov, V. V. (1976). Investigation of the physical and mechanical properties of the lunar sample brought by Luna-20 and along the route of motion of Lunokhod 2. In L. G. Napolitano, et al. (Eds.), *Space Activity Impact on Science and Technology* (pp. 321-332). Oxford: Pergamon. https://doi.org/10.1016/B978-0-08-020365-2.50031-7

Leovy, C. (2001). Weather and climate on Mars. *Nature*, *412*(6843), 245–249. https://doi.org/10.1038/35084192

Li, C., Zheng, Y. K., Wang, X., Zhang, J. H., Wang, Y. B., Chen, L., Zhang, L., Zhao, P., Liu, Y. K., … Wu, F. Y. (2022). Layered subsurface in Utopia Basin of Mars revealed by Zhurong rover radar. *Nature*, *610*(7931), 308–312. https://doi.org/10.1038/s41586-022-05147-5

Li, C. L., Liu, J. J., Ren, X., Zuo, W., Tan, X., Wen, W. B., Li, H., Mu, L. L., Su, Y., … Ouyang, Z. Y. (2015). The Chang'e 3 mission overview. *Space Sci. Rev.*, *190*(1), 85–101. https://doi.org/10.1007/s11214-014-0134-7

Liu, J. J., Li, C. L., Zhang, R. Q., Rao, W., Cui, X. F., Geng, Y., Jia, Y., Huang, H., Ren, X., … Zhang, H. B. (2022). Geomorphic contexts and science focus of the Zhurong landing site on Mars. *Nat. Astron.*, *6*(1), 65–71. https://doi.org/10.1038/s41550-021-01519-5

Liu, Z. Q., Di, K. C., Peng, M., Wan, W. H., Liu, B., Li, L. C., Yu, T. Y., Wang, B. F., Zhou, J. L., and Chen, H. M. (2015). High precision landing site mapping and rover localization for Chang'e-3 mission. *Sci. China Phys. Mech. Astron.*, *58*(1), 1–11. https://doi.org/10.1007/s11433-014-5612-0

Liu, Z. Q., Di, K. C., Li, J., Xie, J. F., Cui, X. F., Xi, L. H., Wan, W. H., Peng, M., Liu, B., … Liu, J. G. (2020). Landing site topographic mapping and rover localization for Chang'e-4 mission. *Sci. China Inf. Sci.*, *63*(4), 140901. https://doi.org/10.1007/s11432-019-2796-1

Mason, C. C., and Nordmeyer, E. F. (1969). An empirically derived erosion law and its application to lunar module landing. *GSA Bull.*, *80*(9), 1783–1788. https://doi.org/10.1130/0016-7606(1969)80[1783:AEDELA]2.0.CO;2

Mason, C. C. (1970). Comparison of actual versus predicted lunar surface erosion caused by Apollo 11 descent engine. *GSA Bull.*, *81*(6), 1807–1812. https://doi.org/10.1130/0016-7606(1970)81[1807:COAVPL]2.0.CO;2

McDivitt, J. A. (1971). *Apollo 15 Mission Report*. Houston, TX: Manned Spacecraft Center.

Mehta, M., Renno, N., Cotel, A., and Grover, M. (2007). Characterization of the impingement dynamics of pulsed rocket plumes with the ground at low ambient pressure. In *43rd AIAA/ASME/SAE/ASEE Joint Propulsion Conference & Exhibit*. Cincinnati, OH: American Institute of Aeronautics and Astronautics. https://doi.org/10.2514/6.2007-5707

Mehta, M., Renno, N. O., Grover, R. M., and Sengupta, A. (2008). Erosion dynamics during phoenix landing on mars. In *AGU Fall Meeting Abstracts*. AGU.

Mehta, M., Sengupta, A., Pokora, M., Hall, L., and Renno, N. (2010). Mars landing engine plume impingement ground interaction. In G. B. Song, et al. (Eds.), *Earth and Space 2010* (pp. 143-157). Honolulu, Hawaii, United States: American Society of Civil Engineers. https://doi.org/10.1061/41096(366)17

Mehta, M., Renno, N. O., Marshall, J., Rob Grover, M., Sengupta, A., Rusche, N. A., Kok, J. F., Arvidson, R. E., Markiewicz, W. J., … Smith, P. H. (2011). Explosive erosion during the Phoenix landing exposes subsurface water on Mars. *Icarus*, *211*(1), 172–194. https://doi.org/10.1016/j.icarus.2010.10.003

Mehta, M., Sengupta, A., Renno, N. O., Norman, J. W. V., Huseman, P. G., Gulick, D. S., and Pokora, M. (2013). Thruster plume surface interactions: applications for spacecraft landings on planetary bodies. *AIAA J.*, *51*(12), 2800–2818. https://doi.org/10.2514/1.J052408

Mehta, M. (2019). Rocket plume interactions for NASA landing systems. Presented at the NASA - DLR Technical Interchange Meeting. Retrieved from https://ntrs.nasa.gov/api/citations/20200000979/downloads/20200000979.pdf.

Mehta, M., Manginelli, M., Liever, P. A., Gale, M., Westra, D., and Thomas, O. (2019). Simulation of insight plume induced surface cratering and validation through imagery based 3D topology reconstruction. In *16th International Planetary Probe Workshop (IPPW)*. Oxford.

Metzger, P. T., Latta, R. C., Schuler, J. M., Immer, C. D., Nakagawa, M., and Luding, S. (2009a). Craters formed in granular beds by impinging jets of gas. *AIP Conf. Proc.*, *1145*(1), 767–770. https://doi.org/10.1063/1.3180041

Metzger, P. T., Li, X. Y., Immer, C., and Lane, J. (2009b). ISRU implications for lunar and Martian plume effects. In *47th AIAA Aerospace Sciences Meeting including The New Horizons Forum and Aerospace Exposition*. Orlando, Florida: American Institute of Aeronautics and Astronautics. https://doi.org/10.2514/6.2009-1204

Metzger, P. T., Immer, C. D., Donahue, C. M., Vu, B. T., Latta, R. C., and Deyo-Svendsen, M. (2009c). Jet-induced cratering of a granular surface with application to lunar spaceports. *J. Aerosp. Eng.*, *22*(1), 24–32. https://doi.org/10.1061/(ASCE)0893-1321(2009)22:1(24

Metzger, P. T., Lane, J. E., Immer, C. D., Gamsky, J. N., Hauslein, W., Li, X. Y., Latta III, R. C., and Donaue, C. M. (2010). Scaling of erosion rate in subsonic jet experiments and Apollo lunar module landings. In G. B. Song, et al. (Eds.), *Earth and Space 2010* (pp. 191-207). Honolulu, Hawaii, United States: American Society of Civil Engineers. https://doi.org/10.1061/41096(366)21

Metzger, P. T., Smith, J., and Lane, J. E. (2011). Phenomenology of soil erosion due to rocket exhaust on the Moon and the Mauna Kea lunar test site. *J. Geophys. Res.: Planets*, *116*(E6), E06005. https://doi.org/10.1029/2010JE003745

Metzger, P. T., and Mantovani, J. G. (2021). The damage to lunar orbiting spacecraft caused by the ejecta of lunar landers. In P. J. van Susante, et al. (Eds.), *Earth and Space 2021* (pp. 136-145). American Society of Civil Engineers. https://doi.org/10.1061/9780784483374.014

Mitchell, J. K., Bromwell, L. G., Carrier, W. D., Costes, N. C., and Scott, R. F. (1972). Soil mechanical properties at the Apollo 14 site. *J. Geophys. Res.*, *77*(29), 5641–5664. https://doi.org/10.1029/JB077i029p05641

Moore, H. J., and Jakosky, B. M. (1989). Viking landing sites, remote-sensing observations, and physical properties of Martian surface materials. *Icarus*, *81*(1), 164–184. https://doi.org/10.1016/0019-1035(89)90132-2

Oravec, H. A., Asnani, V. M., Creage, C. M., and Moreland, S. J. (2021). Geotechnical review of existing mars soil simulants for surface mobility. In P. J. van Susante, et al. (Eds.), *Earth and Space 2021* (pp. 157-170). American Society of Civil Engineers. https://doi.org/10.1061/9780784483374.016

Pla-García, J., Rafkin, S. C. R., Martinez, G. M., Vicente-Retortillo, Á., Newman, C. E., Savijärvi, H., de la Torre, M., Rodriguez-Manfredi, J. A., Gómez, F., … Harri, A. M. (2020). Meteorological predictions for *Mars 2020 Perseverance Rover* landing site at Jezero Crater. *Space Sci. Rev.*, *216*(8), 148. https://doi.org/10.1007/s11214-020-00763-x

Plemmons, D. H., Mehta, M., Clark, B. C., Kounaves, S. P., Peach, L. L., Renno, N. O., Tamppari, L., and Young, S. M. M. (2008). Effects of the Phoenix Lander descent thruster plume on the Martian surface. *J. Geophys. Res.: Planets*, *113*(E3), E00A11. https://doi.org/10.1029/2007JE003059

Rahimi, A., Ejtehadi, O., Lee, K. H., and Myong, R. S. (2020). Near-field plume-surface interaction and regolith erosion and dispersal during the lunar landing. *Acta Astronaut.*, *175*, 308–326. https://doi.org/10.1016/j.actaastro.2020.05.042

Rajaratnam, N. (1982). Erosion by submerged circular jets. *Jo. Hydraul. Div.*, *108*(2), 262–267. https://doi.org/10.1061/JYCEAJ.0005821

Rennó, N. O., Bos, B. J., Catling, D., Clark, B. C., Drube, L., Fisher, D., Goetz, W., Hviid, S. F., Keller, H. U., … Young, S. M. M. (2009). Possible physical and thermodynamical evidence for liquid water at the Phoenix landing site. *J. Geophys. Res.: Planets*, *114*(E1), E00E03. https://doi.org/10.1029/2009JE003362

Roberson, F. I., and Scott, R. F. (1968). Soil mechanics surface sampler. Washington: National Aeronautics and Space Administration.

Roberts, L. (1963). Visibility and dust erosion during the lunar landing. In NASA Langley Research Center (Ed.), *A Compilation of Recent Research Related to the Apollo Mission* (pp. 155-170).

Romine, G. L., Reisert, T. D., and Gliozzi, J. (1973). *Site Alteration Effects from Rocket Exhaust Impingment During A Simulated Viking Mars Landing*. *Part 1*: *Nozzle Development and Physical Site Alternation*. Washington: National Aeronautics and Space Administration.

Scott, R. F., and Ko, H. Y. (1968). Transient rocket-engine gas flow in soil. *AIAA J.*, *6*(2), 258–264. https://doi.org/10.2514/3.4487

Scott, R. F., and Roberson, F. I. (1968). Soil mechanics surface sampler: lunar surface tests, results, and analyses. *J. Geophys. Res.*, *73*(12), 4045–4080. https://doi.org/10.1029/JB073i012p04045

Scott, R. F., Carrier, W. D., Costes, N. C., and Mitchell, J. K. (1971). Apollo 12 soil mechanics investingation. *Géotechnique*, *21*(1), 1–14. https://doi.org/10.1680/geot.1971.21.1.1

Sengupta, A., Kulleck, J., Sell, S., Van Norman, J., Mehta, M., and Pokora, M. (2009). Mars Lander Engine plume impingement environment of the Mars Science Laboratory. In *2009 IEEE Aerospace Conference* (pp. 1-10). Big Sky, MT, USA: IEEE. https://doi.org/10.1109/AERO.2009.4839345

Shaw, A., Arvidson, R. E., Bonitz, R., Carsten, J., Keller, H. U., Lemmon, M. T., Mellon, M. T., Robinson, M., and Trebi-Ollennu, A. (2009). Phoenix soil physical properties investigation. *J. Geophys. Res.: Planets*, *114*(E1), E00E05. https://doi.org/10.1029/2009JE003455

Shorthill, R. W., Hutton, R. E., Moore, H. J., Scott, R. F., and Spitzer, C. R. (1976a). Physical properties of the Martian surface from the Viking 1 lander: preliminary results. *Science*, *193*(4255), 805–809. https://doi.org/10.1126/science.193.4255.805

Shorthill, R. W., Moore, H. J., Hutton, R. E., Scott, R. F., and Spitzer, C. R. (1976b). The environs of Viking 2 lander. *Science*, *194*(4271), 1309–1318. https://doi.org/10.1126/science.194.4271.1309

Smith, P. H., Tamppari, L. K., Arvidson, R. E., Bass, D., Blaney, D., Boynton, W. V., Carswell, A., Catling, D. C., Clark, B. C., … Zent, A. P. (2009). H_2O at the phoenix landing site. *Science*, *325*(5936), 58–61. https://doi.org/10.1126/science.1172339

Spohn, T., Hudson, T. L., Marteau, E., Golombek, M., Grott, M., Wippermann, T., Ali, K. S., Schmelzbach, C., Kedar, S., … Banerdt, W. B. (2022a). The InSight HP³ penetrator (Mole) on mars: soil properties derived from the penetration attempts and related activities. *Space Sci. Rev.*, *218*(8), 72. https://doi.org/10.1007/s11214-022-00941-z

Spohn, T., Hudson, T. L., Witte, L., Wippermann, T., Wisniewski, L., Kedziora, B., Vrettos, C., Lorenz, R. D., Golombek, M., … Grygorczuk, J. (2022b). The InSight-HP³ mole on Mars: lessons learned from attempts to penetrate to depth in the Martian soil. *Adv. Space Res.*, *69*(8), 3140–3163. https://doi.org/10.1016/j.asr.2022.02.009

Surkov, Iu. A., Shandor, V. V., Toporov, Iu. P., Cherkasov, I. I., and Zhuravlev, L. T. (1975). Results of an investigation of contact-mechanical properties of the lunar ground. *Kosm. Issled.*, *13*, 923-931.

Taylor, L. A., Pieters, C. M., and Britt, D. (2016). Evaluations of lunar regolith simulants. *Planet. Space Sci.*, *126*, 1–7. https://doi.org/10.1016/j.pss.2016.04.005

Team, R. (1997). Characterization of the Martian surface deposits by the mars pathfinder rover, sojourner. *Science*, *278*(5344), 1765–1768. https://doi.org/10.1126/science.278.5344.1765

Wang, J., Zhang, Y., Di, K. C., Chen, M., Duan, J. F., Kong, J., Xie, J. F., Liu, Z. Q., Wan, W. H., … Wang, Y. X. (2021). Localization of the Chang'e-5 lander using radio-tracking and image-based methods. *Remote Sens.*, *13*(4), 590. https://doi.org/10.3390/rs13040590

Watkins, R., Metzger, P. T., Mehta, M., Han, D. R., Prem, P., Sibille, L., Dove, A., Jolliff, B., Moriarty III, D. P., … Radley, C. F. (2021). Understanding and mitigating plume effects during powered descents on the moon and mars. *Bull. AAS*, *53*(4). https://doi.org/10.3847/25c2cfeb.f9243994

Williams, J. P., Paige, D. A., Greenhagen, B. T., and Sefton-Nash, E. (2017). The global surface temperatures of the Moon as measured by the Diviner Lunar Radiometer Experiment. *Icarus*, *283*, 300–325. https://doi.org/10.1016/j.icarus.2016.08.012

Wu, B., Dong, J., Wang, Y. R., Rao, W., Sun, Z. Z., Li, Z. J., Tan, Z. Y., Chen, Z. Y., Wang, C., … Li, H. L. (2022). Landing site selection and characterization of tianwen-1 (Zhurong rover) on mars. *J. Geophys. Res.: Planets*, *127*(4), e2021JE007137. https://doi.org/10.1029/2021JE007137

Xu, C., Huang, X. Y., Guo, M. W., Li, M. D., Hu, J. C., and Wang, X. L. (2022). End-to-end Mars entry, descent, and landing modeling and simulations for Tianwen-1 guidance, navigation, and control system. *Astrodynamics*, *6*(1), 53–67. https://doi.org/10.1007/s42064-021-0115-z

Xu, W. M., Liu, X. F., Yan, Z. X., Li, L. N., Zhang, Z. Q., Kuang, Y. W., Jiang, H., Yu, H. X., Yang, F., … Shu, R. (2021). The MarSCoDe Instrument suite on the mars rover of China's Tianwen-1 mission. *Space Sci. Rev.*, *217*(5), 64. https://doi.org/10.1007/s11214-021-00836-5

You, J. L., Zhang, X. P., Zhang, H. Y., Li, C. H., Xu, Y., Yan, Q., Yu, H., Liu, J., Li, Y., … Zhi, Q. J. (2021). Analysis of plume-lunar surface interaction and soil erosion during the Chang'E-4 landing process. *Acta Astronaut.*, *185*, 337–351. https://doi.org/10.1016/j.actaastro.2021.05.009

Yu, Z. S., Cui, P. Y., and Crassidis, J. L. (2017). Design and optimization of navigation and guidance techniques for Mars pinpoint landing: review and prospect. *Prog. Aerospace Sci.*, *94*, 82–94. https://doi.org/10.1016/j.paerosci.2017.08.002

Zhang, H. Y., Li, C. H., You, J. L., Zhang, X. P., Wang, Y., Chen, L. P., Fu, Q. F., Zhang, B. G., and Wang, Y. M. (2022). The investigation of plume-regolith interaction and dust dispersal during Chang'E-5 descent stage. *Aerospace*, *9*(7), 358. https://doi.org/10.3390/aerospace9070358

Zhu, D. Y., Lee, C. F., Qian, Q. H., and Chen, G. R. (2005). A concise algorithm for computing the factor of safety using the Morgenstern-Price method. *Can. Geotech. J.*, *42*(1), 272–278. https://doi.org/10.1139/t04-072

Zou, Y. L., Zhu, Y., Bai, Y. F., Wang, L. G., Jia, Y. Z., Shen, W. H., Fan, Y., Liu, Y., Wang, C., … Peng, Y. Q. (2021). Scientific objectives and payloads of Tianwen-1, China's first Mars exploration mission. *Adv. Space Res.*, *67*(2), 812–823. https://doi.org/10.1016/j.asr.2020.11.005